UNIVERSITY OF CALIFORNIA, SAN DIEGO

Multiband Deblurring for Fluid Lens Cameras

A dissertation submitted in partial satisfaction of the
requirements for the degree
Doctor of Philosophy

in

Electrical Engineering (Signal and Image Processing)

by

Jack Tzeng

Committee in charge:

Professor Truong Q. Nguyen, Chair
Professor Serge Belongie
Professor William S. Hodgkiss
Professor Yu-Hwa Lo
Professor Nuno Vasconcelos

2010

The dissertation of Jack Tzeng is approved, and it is acceptable in quality and form for publication on microfilm and electronically:

_____

_____

_____

_____

_____

Chair

University of California, San Diego

2010

DEDICATION

To my parents, my friends, and my colleagues. You each make my defeats softer and my victories sweeter.

EPIGRAPH

It does not matter where you are or what you are doing, it matters who you are with.

—Jack Tzeng

TABLE OF CONTENTS

LIST OF FIGURES

LIST OF TABLES

ACKNOWLEDGEMENTS

I believe that no great accomplishment can be achieved in solitude. Without the support, knowledge, and ideas of many people, this thesis would never have been possible. I have had a full spectrum of contributors and collaborators, ranging from conversations on a white board that may have sparked ideas to co-authors who have helped refine many of the ideas throughout this process.

First, this would not have been possible without my advisor Professor Truong Nguyen. His understanding, knowledge, and drive have helped me throughout the easy and the difficult times of my Ph.D. While his academic support has been substantial, I also consider his advice on life to be invaluable. His management style, predicated on trust and cooperation, is something that I hope to apply to my own life. I am honored to always be his student.

Prof. Yu-Hwa Lo has been a constant figure throughout my Ph.D. career. In collaboration with his group, he has invented and developed the Fluid Lens. He had provided academic advice and ideas regarding the development and physics of the lens system.

I would like to thank my committee of Prof. Serge Belongie, Prof. Bill Hodgekiss, and Prof. Nuno Vasconcelos. Each member has contributed knowledge, insight, and perspective. These contributions provided new and interesting angles to approach various problems. The ideas developed during conversations with each member has helped fuel the various chapters of this thesis.

Pro. Yoav Freund has provided several key components to the Adaboost section of this work. He has always been available to discuss areas of fruitful research. The software support provided by his lab provided efficient ways of developing, analyzing, and understanding his methods. I appreciate the guidance Prof. Freund has offered.

Dr. Frank Tsai has been the chief researcher in the design of the Fluid Lens. By building the hardware components of the lens and providing invaluable test data, his work has helped me understand the nature of the fluid lens problem. I have enjoyed our many discussions about the lens.

I would like to thank my parents Karl and Flora Tzeng as well as my brother

Walker Tzeng. I have always known that despite all else, I will always have their support. I know that they are proud of my accomplishments and I hope that I am a reflection of their love.

The entire Surgicam team has brought this project from ideas to life. Their support includes and is not limited to building the lens, testing the system, and gathering images from pig surgery. With any complex system, each piece is crucial to the success of the entire project. I have enjoyed the support of several members including: Laura Wolszon, Donald Kimball, Douglas Palmer, Daniel Johnson, Cuong Vu, Boz Kamyabi, Mark Talamini, Santiago Horgan, Yoav Mintz, Adam Spivak, Kari Thompson, Cameron Francis, Sung Hwan Cho, and Ash Arianpour. For anyone who I have missed, I apologize. Your support has helped to develop something truly amazing.

I would like to thank the entire UCSD Video Processing Lab past and present. I have enjoyed several enlightening conversations with: Shay Har-Noy, Natan Jacobson, and Stanley Chan. Joel Park and Ramsin Khoshabeh are members of the lab who have contributed significantly to the Surgicam project. The other members of the lab and visiting scholars have each offered contributions to my growth as a student.

The text of Chapter 3 is adapted from *Image Enhancement for Fluid Lens Camera Based on Color Correlation*, Jack Tzeng and Truong Nguyen, in the February 2009 issue of *IEEE Transactions on Image Processing*. The dissertation author was the primary author of these publications, and the co-author listed directed and supervised the research which forms the basis for this chapter.

The text of Chapter 4 is adapted from *Contourlet Domain Multiband Deblurring Based on Color Correlation for Fluid Lens Cameras*, Jack Tzeng, Chun-Chen Liu, and Truong Nguyen, to be published in 2010 in *IEEE Transactions on Image Processing*. The dissertation author was the primary author of these publications, the first co-author listed supplied ideas, and the second co-author listed directed and supervised the research which forms the basis for this chapter.

The text of Chapter 5 is adapted from *Multiband Deblurring using Support Vector Regression for Fluid Lens Cameras*, Jack Tzeng and Truong Nguyen, sub-

mitted February 2010, in preparation for *IEEE Transactions on Image Processing*. The dissertation author was the primary author of these publications, and the co-author listed directed and supervised the research which forms the basis for this chapter.

The text of Chapter 6 is adapted from *Multiband Deblurring using Adaboost for Fluid Lens Cameras Based on Color Correlation*, Jack Tzeng, Yoav Freund, and Truong Nguyen, submitted April 2010, in preparation for *IEEE Transactions on Image Processing*. The dissertation author was the primary author of these publications, the first co-author listed supplied ideas, and the second co-author listed directed and supervised the research which forms the basis for this chapter.

I am grateful for the financial support of the Telemedicine and Advanced Technology Research Center, the Jacobs Foundation, the Von Liebig Foundation, and the UCSD Chancellor's Interdisciplinary Scholarship.

VITA

2006	Bachelor of Science, Electrical Engineering and Computer Science, University of California, Berkeley
2008	Master of Science, Electrical and Computer Engineering, University of California, San Diego
2010	Doctor of Philosophy, Electrical and Computer Engineering, University of California, San Diego

PUBLICATIONS

Jack Tzeng and Truong Q. Nguyen "Using Filter Banks to Enhance Image for Fluid Lens Cameras Based on Color Correlation", *Proceedings of the International Conference on Acoustics, Speech and Signal Processing*, pp. 381-384, April 2009.

Jack Tzeng and Truong Q. Nguyen "Image Enhancement for Fluid Lens Camera Based on Color Correlation", *IEEE Transactions on Image Processing*, vol. 18, pp 729-739, April 2009.

Jack Tzeng and Chun-Chen Liu and Truong Q. Nguyen "Multi-Band Color Image Deblurring Using Contourlets for Fluid Lens Camera Systems", *IEEE International Conference on Image Processing*, pp. 713-716, 2010.

Jack Tzeng, Chun-Chen Liu, and Truong Q. Nguyen "Contourlet Domain Multiband Deblurring Based on Color Correlation for Fluid Lens Cameras", accepted to be published in *IEEE Transactions on Image Processing*, 2010.

Jack Tzeng and Truong Q. Nguyen "Multiband Deblurring using Support Vector Regression for Fluid Lens Cameras", *IEEE Transactions on Image Processing*. Submitted February 2010.

Jack Tzeng, Yoav Freund, and Truong Q. Nguyen "Using Adaboost on Contourlet Based Image Deblurring for Fluid Lens Camera Systems", *IEEE International Conference on Image Processing*. Submitted February 2010.

Jack Tzeng, Yoav Freund, and Truong Q. Nguyen "Multiband Deblurring using Adaboost for Fluid Lens Cameras Based on Color Correlation", *IEEE Transactions on Image Processing*. Submitted April 2010.

ABSTRACT OF THE DISSERTATION

Multiband Deblurring for Fluid Lens Cameras

by

Jack Tzeng

Doctor of Philosophy in Electrical Engineering (Signal and Image Processing)

University of California, San Diego, 2010

Professor Truong Q. Nguyen, Chair

Unique image processing challenges are produced by the Fluid Lens Camera System. Over traditional glass lens systems, better miniaturization potential and fixed length lens while zooming are unique abilities offered by the fluid lens. Non-uniform blurring for each color plane of the image is also caused by the fluid in the lens. A sharp green color plane and blurred blue and red color planes are also produced by this fluid. For natural and medical images, the edges in the green and blue color planes are similar. In this work, the sharpness of the blurred color planes is improved by sharing edge information between color planes. Avoiding shading artifacts while improving edge quality is the goal of this work. Several algorithms are discussed: a wavelet-based algorithm, a contourlet-based algorithm, a Support Vector Regression algorithm, and an Adaboost classification algorithm.

In each algorithm, the strengths of the previous algorithm are built upon in order to improve results. A major advantage of these methods is that shading and edge information is combined without using a complicated point spread function. While the focus of this dissertation is on using the green color plane to improve the blue color plane, the same algorithms could be applied to the red color plane as well. Infrared imaging, medical image overlaying, satellite mapping, and remote sensing are all multiband system with high edge correlation where this work could be applied.

Chapter 1

Introduction

Developed by Lo, the Fluid Lens Camera System (FLCS) [1, 2, 3] is a camera that uses fluid optics instead of glass optics. A much smaller camera than traditional camera systems, the amount of fluid in the lens chamber is adjusted dynamically to control the curvature of each lens. Objects are magnified and focused by altering the curvature of the lens chamber. In addition, the lens is a fixed size and does not telescope while zooming. This property is ideal for surgery because the camera does not consume space in the surgical field. Enticing opportunities for surgical and cellular areas are presented by this lens system. That excitement is tempered by some of the natural disadvantages of the system.

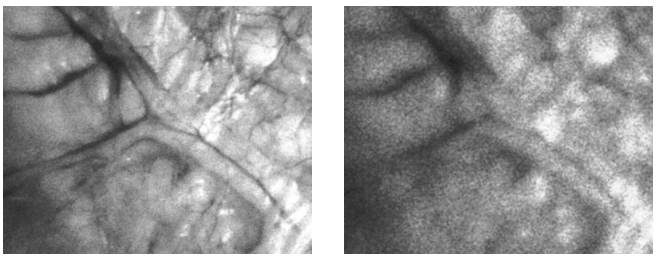

(a) (b)

Figure 1.1: The FLCS blurs two different color planes differently. (a) Green image from the device; (b) blue image from the device.

For the FLCS, one of the major hardware issues is that the fluid causes non-uniform blurring of different color planes. Because of these axial color aberrations, images from certain wavelengths are sharp while images from other wavelengths

are blurred. A focused green image was developed by the camera's inventors at the cost of extremely blurred blue and red images. Shown in Fig. 1.1, different levels of sharpness are seen for the various color planes.

(a)

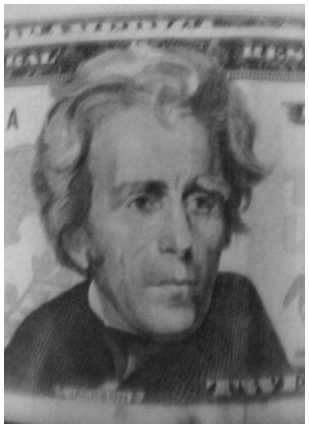

(b)

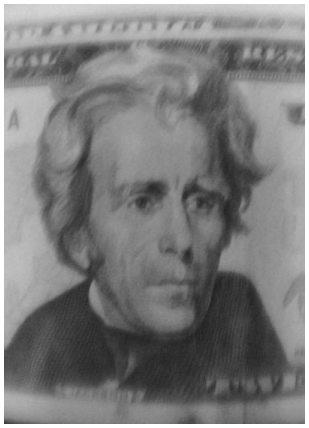

(c)

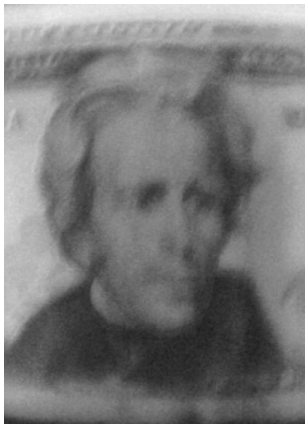

(d)

Figure 1.2: The FLCS has a complicated PSF. (a) The color image; (b) the red image; (c) the green image; (d) the blue image.

A second problem with the FLCS is that the point spread function (PSF) varies with spatial location, object depth, color wavelength, and zoom. The PSF is a measure of the amount of blur caused by the lens. In Fig. 1.2, an example is shown of an image from the lens. Since PSF varies with spatial location, objects in

the center of the image appear sharper than objects along the perimeter. The PSF varies with color wavelength, with green appearing sharpest. Due this variability, a PSF is difficult to estimate and prone to severe estimation error.

The basic image inverse problem [4] is seen in (1.1).

$$\hat{B}(x) = L_0(x) * B(x) + N(x) \tag{1.1}$$

B is the original sharp blue image, x is the spatial location, N is the noise, $*$ is the convolution operator, L_0 is the lens, and $\hat{B}$ is the output image after it has been blurred by the lens.

An accurate PSF estimation is a crucial piece of conventional image processing methods [5, 6] such as the Lucy-Richardson deconvolution algorithm [7, 8] and the Wiener deconvolution algorithm [9]. The PSF for the FLCS has several variables. The effectiveness of these algorithms is limited by the estimation errors with the PSF.

To address these hardware issues, novel image processing solutions are proposed which do not require a PSF. By examining the edge characteristics of the green color plane, knowledge is gained about the structure and edge characteristics of the overall system. This knowledge is applied to the other color planes and a sharper, more consistent color image is produced. Four different methods are discussed to enhance these color images. The common theme for each of these algorithms is to balance the restrictive PSF of the FLCS against the natural sharpness information provided by the green color plane.

The first method is the Wavelet Sub-band Meshing algorithm [10, 11]. Adapting a technique for image demosaicking [12, 13], much less channel knowledge and fewer tuning parameters are required by this method. This algorithm is extremely efficient and significant gains in image quality are produced. The correlation between the edges of the green image and edges of the red and blue images [14, 15] is the foundation of this method. The best results are achieved when natural sharp objects have similar edge direction in the red, green, and blue color planes. Color bleeding artifacts are produced when objects in the image do

not have similar edge direction. Successful results in the surgical arena are produced because of the similarity in edge direction between the green and blue color planes.

The Contourlet Sub-band Meshing algorithm is the second method presented [16]. Contourlets [17, 18] rather than wavelets [19, 20] are relied upon by this algorithm to produce sharp natural edges. Similar edge correlation problems are produced by the contourlet algorithm. However, the effects of color bleeding are much less noticeable. The directional filters of the contourlet-based method are used to adjust to the natural contours of the image. Edges in the blue and red color planes are produced by this adjustment. The structure of the original object is maintained.

The Support Vector Regression (SVR) algorithm is the third algorithm presented. In the previous two methods, the color bleeding issue is not dealt with effectively. A bank of sharp medical images is used to train the SVR algorithm to produce a regression model [21, 22]. Areas of weak and strong edge correlation are identified by this regression model and the proper coefficients are predicted. Color bleeding artifacts are reduced while the same level of sharpness is maintained.

The Adaboost method is the fourth algorithm presented. By manipulating several weak classifiers, a strong classifier is produced by Adaboost. The goal of this classification is to differentiate between three component methods: the Contourlet Sub-band Meshing algorithm, the Color SVR and the Edge SVR. Features such as derivatives in the color domain, derivatives in the spatial domain, pixel values, and contourlet coefficients are used to discriminate between the three methods. At each pixel location, one of the three methods is selected by the strong classifier. This method is the classifier's prediction as to which of the three methods will produce the strongest result. The results of this prediction are combined to produce an image which has lower error than each of the three component methods.

1.1 Review of Fluid Lens Camera System Color Blur

Two fluid lens chambers are contained in the FLCS. This fluid lens design is modeled after natural eye systems. A major problem for the lens is that different color wavelengths react non-uniformly to the fluid and axial color aberrations are produced.

As a design choice, a Bayer Pattern is used by the CMOS sensor. The Bayer pattern samples green values at twice the rate that the red and blue color planes are sampled. In order to maximize the number of sharp samples, the device is tuned to sharpen the green color plane. While a sharp green image is produced by this tuning, blurred red and blue images are also produced.

In traditional glass lens systems, the conventional approach to dealing with these axial color aberrations in hardware is to design doublets or triplets where lenses are fitted together. The natural color dispersion of the glass material is compensated for by these acromats. Because of the difficulty inherent in designing the two lenses, fitting doublets or triplets to the FLCS becomes infeasible to model. At this stage of prototyping, image processing solutions are the most effective means with which to address these axial color aberrations.

1.2 Notation

This thesis uses the following notation:

$\hat{B}$	The $\hat{}$ represents an estimate of B after it passes through a lens.
$\widehat{BLH}$	The sub-band output after filtering and down-sampling $\hat{B}$ twice. Here, an L and an H represent a low-pass and a high-pass filter at each level respectively.
$\widehat{GLH}$	Similar to $\widehat{BLH}$, $\widehat{GLH}$ comes from the output $\widehat{G}$ from the lens of the Green component. Here, an L and an H represent

	a low-pass and a high-pass filter at each level respectively. $\widehat{RLH}$ is associated with the Red component.
$\widehat{B}_r$	The subscript $_r$ represents an output after reconstruction of $\widehat{B}$.
$\widehat{B}_{rL}$	The subscript $_L$ represents the low frequency sub-band output of $\widehat{B}_r$.
$\widehat{G}_{rH}$	The subscript $_H$ represents the high frequency sub-band output of $\widehat{G}_r$.
E_G	The error in estimating G.
$x \approx y$	The $\approx$ notation means that $\lvert x - y \rvert < 2^{-10}$.
$\tilde{B}$	The $\tilde{.}$ represents the reconstruction estimate for a given algorithm.
B_f	The subscript f represents the frequency response of B.
ω_1, ω_2	The spatial frequency.
L_0	The PSF of the lens.
$\tilde{B}_i$	The intermediate output from one of three methods used by Adaboost $i \in \{1, 2, 3\}$.

Chapter 2

Previous Methods

For the past century, conventional hardware approaches were developed to address axial color aberrations. Sets of doublets or triplets were fitted and designed together to reduce this distortion. In the FLCS, only two lens chambers are used. Due to the variations in blur from the unusual PSF, the system is difficult to model. Attempting to fit and model several fluid lenses becomes intractable.

2.1 Conventional Methods

Instead of dealing with this problem in hardware, software approaches are proposed. The three basic methods for deblurring are: Wiener deconvolution [9] in the presence of Additive White Gaussian Noise (AWGN), Lucy-Richardson deconvolution [8, 7] in the presence of Poisson noise, and Total Variation [23] to accomplish joint denoising and deblurring.

In Wiener deconvolution, the blur of the lens is directly inverted in the frequency domain:

$$H_f(\omega_1, \omega_2) = \frac{|L_{f0}(\omega_1, \omega_2)|^2}{|L_{f0}(\omega_1, \omega_2)|^2 + \frac{N_f(\omega_1, \omega_2)}{B_f(\omega_1, \omega_2)}} \tag{2.1}$$

$$\tilde{B}_f(\omega_1, \omega_2) = \frac{H_f(\omega_1, \omega_2)\hat{B}_f(\omega_1, \omega_2)}{L_{f0}(\omega_1, \omega_2)} \tag{2.2}$$

Here, L_{f0} is the frequency response of the PSF and $\frac{N_f(\omega_1,\omega_2)}{B_f(\omega_1,\omega_2)}$ is the noise-to-signal ratio. Without noise, $H_f = 1$ and this method becomes a standard inverse filter. When $|L_{f0}(\omega_1, \omega_2)|$ has zero locations, the frequency values are unrecoverable.

In the image processing domain, the second conventional deblurring approach is the Lucy-Richardson algorithm. The Lucy-Richardson method is an iterative approach which assumes a Poisson noise statistic.

$$\tilde{B}^{k+1}(x) = \tilde{B}^k(x) * L_0(x) * \frac{\hat{B}(x)}{L_0(x) * \tilde{B}^k(x)} \tag{2.3}$$

k is the iteration step and x is the spatial location. The PSF is an estimate of how the fluid lens blurs light before the CMOS sensor registers the image.

With a good estimate of the PSF, the Lucy-Richardson algorithm converges to the maximum likelihood solution assuming a Poisson counting statistic [24]. Even when natural images do not follow this statistic, if the PSF and input image are non-negative, then the output image is non-negative. Compared to other algorithms, the necessity to clip or normalize negative outputs is avoided.

To use this algorithm for the FLCS, an estimate of the PSF is required for each color plane. A unique PSF is applied to each of the three color planes [4, 25, 26]. While the PSF for the blue and red color planes are very large due to the amount of blurring caused by the lens, the PSF for the green image would be close to a 2-D delta function.

A major contribution of this work is that the proposed algorithms do not require an estimate of the PSF. Errors caused during estimation are avoided. As discussed in Chapter 1, the PSF is a function of several different parameters. Using the Lucy-Richardson algorithm or the Wiener deconvolution algorithm is computationally expensive because of the variable nature of the PSF. The proposed algorithms do not require this error-prone step.

An alternative approach would be to transform the RGB image to another domain such as YCrCb. In this domain, most of the edge information is contained in the Luma component while most of the color and shading information is contained in the Chroma components. Since blurring has only a minor affect

on the Chroma components, deblurring using the Lucy-Richardson algorithm is performed only on the Luma component. A consistent level of blurring between the three color planes is implicitly assumed by this method. For the FLCS, this assumption does not hold.

In Fig. 2.1(a) and Fig. 2.1(c), sample images taken by the lens are shown. In Fig. 2.1(b) and Fig. 2.1(d), the same images are shown after ten iterations of the Lucy-Richardson algorithm run on the luminance in the YCbCr domain. While Fig. 2.1(b) has sharper edges and less noise, moderate improvement is seen in Fig. 2.1(d).

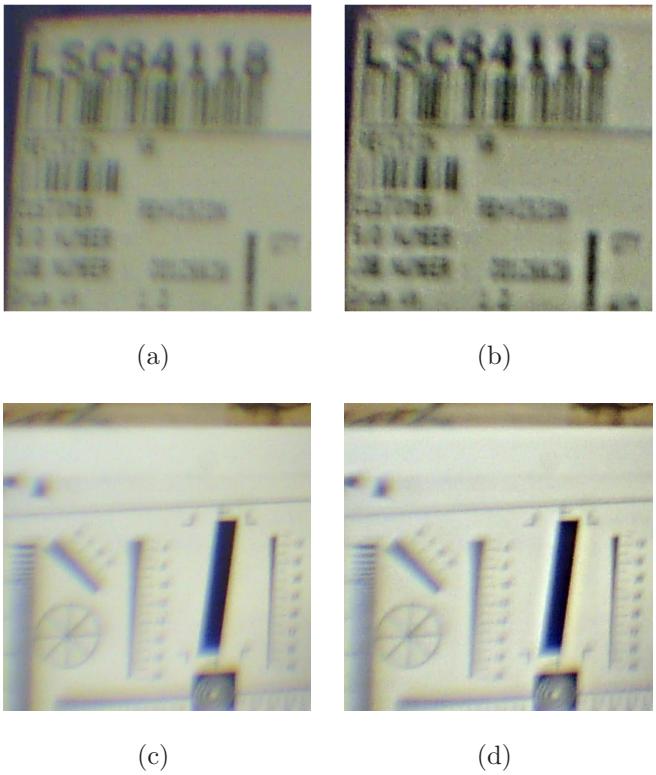

(a) (b)

(c) (d)

Figure 2.1: The Lucy-Richardson algorithm has both successful and moderate deblurring results after running ten iterations on the Luma component. (a) First original image; (b) successful deblurring of first image; (c) second original image; (d) moderate deblurring of second image.

The Total Variation deconvolution method [23] is a more recent attempt at denoising and deblurring. The Alternating Minimization algorithm [27] is used to implement this approach efficiently. Similar to Wiener deconvolution, the Total

Variation is dependent on an accurate PSF estimation. The success of this approach is limited by the estimation errors. This limitation makes it inappropriate for the FLCS.

2.2 Additive Wavelet RGB

In the field of Remote Sensing, one of the major goals is to develop pan-sharpening algorithms. In the problem setup, low resolution color or multi-spectral images and high resolution pan-chromatic or single-spectral images are provided. The goal of pan-sharpening is to fuse the two data sources to provide a high resolution multi-spectral image.

Several techniques exist for pan-sharpening [28]. For many of these algorithms, the image is transformed to the color image to the intensity-hue-saturation domain. The intensity component of the image is processed. By processing the intensity component, these algorithms avoid biasing the end result toward gray colors. A review of these methods can be found in [28].

One of the methods which is similar to the proposed wavelet method discussed in Chapter 3 is the Additive Wavelet Luminance (AWL) and Additive Wavelet RGB (AWRGB) methods [29]. In the AWRGB method, the pan-chromatic image is decomposed into n wavelet resolution levels:

$$P = w_{p0} + \sum_{i=1}^{n} w_{pi} \tag{2.4}$$

Here, w_{p0} is the lowest resolution wavelet sub-band and w_{pi} is the higher sub-band. Over the color images, higher edge fidelity and resolution is contained in the pan-chromatic image. The edge information stored in the pan-chromatic image is characterized in the second term, $\sum_{i=1}^{n} w_{pi}$. In the AWRGB method, the edge information is added to the original color images:

$$R' = R + \sum_{i=1}^{n} w_{pi} \tag{2.5}$$

$$G' = G + \sum_{i=1}^{n} w_{pi} \tag{2.6}$$

$$B' = B + \sum_{i=1}^{n} w_{pi} \tag{2.7}$$

Note that the R, G, and B images are used directly during the wavelet reconstruction process. The original color details of the multi-spectral image are preserved by this method while including the edge information from the pan-chromatic images. A similar addition of the pan-chromatic details is produced by the AWL method. However, only the Luminance or Intensity component of the multi-spectral image is processed.

2.3 Image Modeling

In the area of Image Denoising, various methods are proposed to model the natural statistics of images. With an accurate model, the noise and the signal can be separated. The task of image denoising is simplified. A Gaussian Scale Mixture Model in the wavelet domain are proposed to address this issues [30, 31, 32]. This model has the advantage of high kurtosis marginal distributions, and positive covariance between the neighboring coefficient amplitude. A cluster of coefficients can be modeled as a Gaussian vector scaled by an unknown factor. A more complete review of this method can be found in [31].

In [33], Dark Flash Photography is presented as a multiband application. An infrared flash is used to capture edges in low light conditions. The advantage of an infrared flash is that the edges of an object can be captured. However, the flash is less noticeable to the people in the scene. The edge information is then applied to the RGB images in order to produce a sharp image in a dark setting with natural colors and a dimmer flash than a traditional camera. The goal of this is to produce a reconstructed image with the edge fidelity of the infrared

image and the color intensity similar to the denoised version of the RGB image. This problem is framed as a minimization problem. The goal of the algorithm is to minimize a combination of several weighted terms including: the difference between the reconstruction and the RGB image, the gradient of the reconstruction, and the difference between the gradient of the reconstruction and the gradient of the infrared image.

In [33], models are explored which exploit dependencies between color channels. K-SVD denoising from [34] and fields-of-experts from [35, 36] are included in these models. The major issues with developing image priors is that images tend to have a high-dimensionality, and the structure of an object can extend over a large window. Explicit spectral models are proposed by [37, 38]. The various dependencies and correlations between different spectral bands are explored in these models.

Chapter 3

Wavelet Sub-band Meshing

The Wavelet Sub-band Meshing algorithm is a first attempt at recognizing and dealing with the deficiencies of previous work. The major problems addressed by this work are: the over-reliance of previous methods on accurate PSF estimation, the computation resources needed by iterative approaches such as the Lucy-Richardson algorithm, and the inability of previous work to recognize the non-uniform blurring of color planes caused by the liquid lens.

In Fig. 2.1, the possibilities and limitations of the Lucy-Richardson algorithm are shown. The lack of complete utilization of the blur characteristics of the FLCS are a limiting factor for this algorithm. With the configuration of the FLCS, the green color planes are sharp and the blue and red color planes are blurred. Unlike previous methods, an algorithm which uses this information to improve blurred color planes is proposed. The edges of the resulting color image are enhanced.

For most natural color images, high edge correlation is exhibited in the red, green, and blue (RGB) color planes (Fig. 3.1) [12, 13]. However, distinct shading characteristics are also contained in the natural images [39]. For the FLCS, different amounts of blur are experienced by the different color planes. In [10, 11], a perfect reconstruction filter bank is modified to improve the blue image resolution by using green image edge information.

In a standard perfect reconstruction filter bank, a signal is decomposed into separate sub-bands [20]. The result is reconstructed back to the original signal.

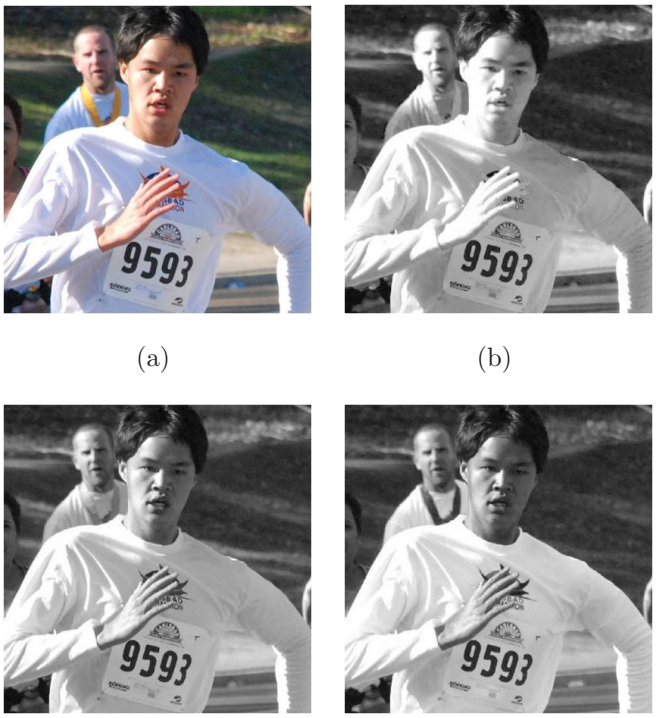

Figure 3.1: This image shows a natural image where different color planes have similar edge characteristics, but different shading levels. (a) Color image; (b) red image; (c) green image; (d) blue image.

In Fig. 3.2, the original signal is blurred by the lens L_0. As a result, the blurred signal $\hat{B}$ is reconstructed by the filter bank. Here, the shading information is represented by the sub-band $\widehat{BLL}$ while the edge information is represented by the $\widehat{BLH}$, $\widehat{BHL}$ and $\widehat{BHH}$.

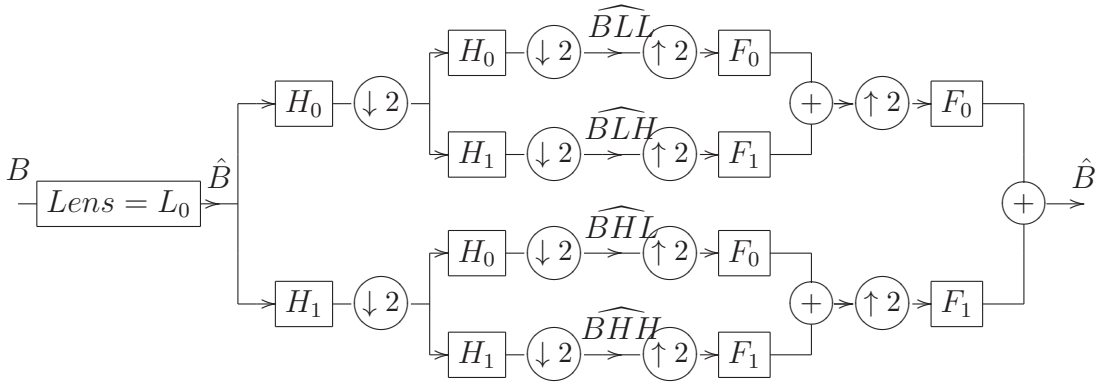

Figure 3.2: A standard perfect reconstruction filter bank is shown.

In the proposed system (Fig. 3.3), the edge sub-bands of the blue image are replaced with the edge sub-bands of the green image. Due to blurring, distorted edge information is contained in the $\widehat{BHL}$, $\widehat{BLH}$, and $\widehat{BHH}$ sub-bands. The blue shading is maintained in the $\widehat{BLL}$ sub-band. Estimates of the edges are contained in the $\widehat{GLH}$, $\widehat{GHL}$, and $\widehat{GHH}$ sub-bands. As the level of blur is increased, the number of levels of decomposition is increased and more green edge information is used.

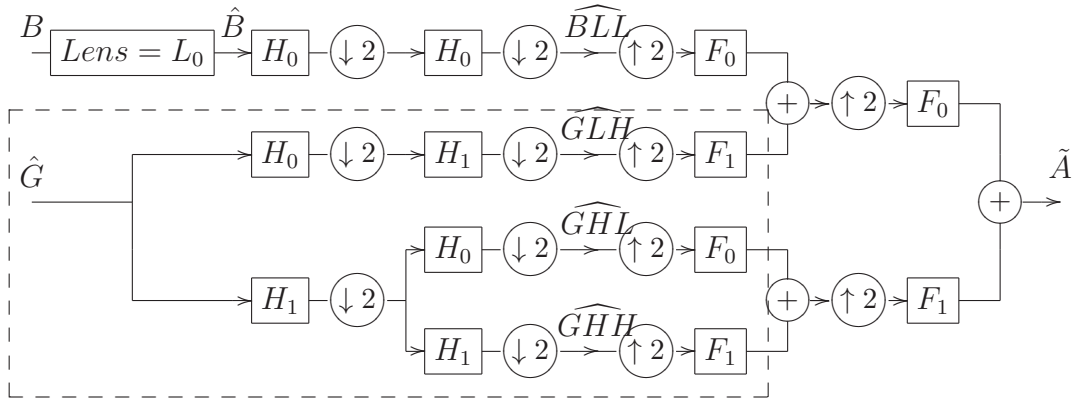

Figure 3.3: A reconstruction filter bank is modified to take the edge information from the green image and shading information from the blue image.

The inputs to the system are a low quality blue image and a high quality

green image:

1. Select a perfect reconstruction filter bank.
2. Decompose the images into four sub-bands by first filtering and down-sampling the rows, then filtering and down-sampling the columns.
3. Replace the band pass sub-bands of the blue image ($\widehat{BLH}$, $\widehat{BHL}$, $\widehat{BHH}$) with the band pass sub-bands of the green image ($\widehat{GLH}$, $\widehat{GHL}$, $\widehat{GHH}$).
4. Depending on the degree of blur, introduce more levels of decomposition by further down-sampling and filtering the $\widehat{BLL}$ component. The green color sub-bands will replace more of the corresponding blue color sub-bands.
5. Reconstruct by up-sampling and filtering.

3.1 Analysis of the Algorithm

For clarity, the one dimensional case is shown in this analysis. The two dimensional case is a natural extension of this work. All filters are assumed to have unit gain at DC.

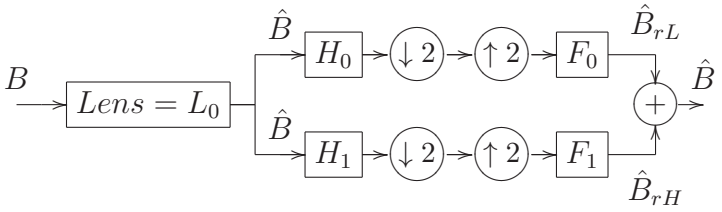

Figure 3.4: Blurring with L_0 followed by a standard one dimensional perfect reconstruction filter bank are shown.

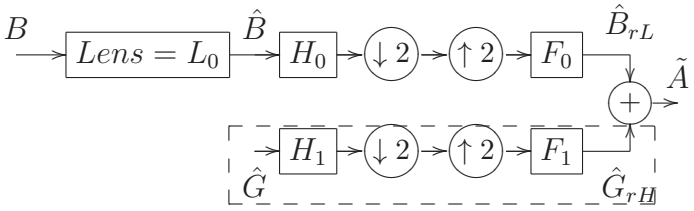

Figure 3.5: A one dimensional modified reconstruction filter bank is shown.

In Fig. 3.4, the blurring effects of the lens on the true blue image $B(z)$ is modeled by L_0 as a low-pass filter.

$$\hat{B}(z) = L_0(z)B(z) \tag{3.1}$$

In Fig. 3.4, a standard filter bank is shown after the lens:

$$\hat{B}_{rL}(z) = \frac{1}{2}F_0(z)(H_0(z)\hat{B}(z) + H_0(-z)\hat{B}(-z)) \tag{3.2}$$

$$\hat{B}_{rH}(z) = \frac{1}{2}F_1(z)(H_1(z)\hat{B}(z) + H_1(-z)\hat{B}(-z)) \tag{3.3}$$

Modifying this filter bank, $\hat{B}_{rH}(z)$ is replaced with $\hat{G}_{rH}(z)$ from the green image sub-band of Fig. 3.5:

$$\hat{G}_{rH}(z) = \frac{1}{2}F_1(z)(H_1(z)\hat{G}(z) + H_1(-z)\hat{G}(-z)) \tag{3.4}$$

In order to reconstruct the original signal B, the higher sub-bands of the $\hat{B}$ are replaced with the higher sub-bands of $\hat{G}$. From the optical properties of the lens, the higher sub-bands $\hat{G}$ are assumed to estimate the edges of B more closely than the higher sub-bands of $\hat{B}$:

$$\begin{aligned} &H_1(z)\hat{G}(z) + H_1(-z)\hat{G}(-z) + E_G \\ &\quad = H_1(z)B(z) + H_1(-z)B(-z) \end{aligned} \tag{3.5}$$

$$\begin{aligned} &H_1(z)\hat{B}(z) + H_1(-z)\hat{B}(-z) + E_B \\ &\quad = H_1(z)B(z) + H_1(-z)B(-z) \end{aligned} \tag{3.6}$$

$$|E_G| \leq |E_B| \tag{3.7}$$

Estimates of the true high-pass sub-bands of B are represented in equations (3.5) and (3.6), where E_G and E_B are the errors of the two estimates. Because of high edge correlation, that inequality (3.7) is assumed to hold.

The green color sub-bands are used to create our reconstructed image $\tilde{A}(z)$:

$$\begin{aligned}
\tilde{A}(z) &= \hat{B}_{rL}(z) + \hat{G}_{rH}(z) && (3.8)\\
&= \frac{1}{2}(F_0(z)(H_0(z)\hat{B}(z) + H_0(-z)\hat{B}(-z))) \\
&\quad + \frac{1}{2}(F_1(z)(H_1(z)B(z) + H_1(-z)B(-z))) \\
&\quad - \frac{1}{2}F_1(z)E_G && (3.9)\\
&= \frac{1}{2}[F_0(z)H_0(z)L_0(z)B(z) \\
&\quad + F_0(z)H_0(-z)L_0(-z)B(-z) \\
&\quad + F_1(z)H_1(z)B(z) + F_1(z)H_1(-z)B(-z) \\
&\quad - F_1(z)E_G] && (3.10)
\end{aligned}$$

Ideally, if the aliasing component $B(-z)$ can be removed, then a delayed version of the original signal $B(z)$ can be reconstructed. The following reconstruction conditions are produced:

$$F_0(z)H_0(z)L_0(z) + F_1(z)H_1(z) = 2z^{-l} \quad (3.11)$$

$$F_0(z)H_0(-z)L_0(-z) + F_1(z)H_1(-z) = 0 \quad (3.12)$$

$$|F_1(z)E_G| = \epsilon \quad (3.13)$$

$H_0(z)$ and $L_0(z)$ are both low-pass filters. If $H_0(z)$ has a lower transition frequency than that of $L_0(z)$, then the following two approximations hold.

$$H_0(z)L_0(z) \approx H_0(z) \quad (3.14)$$

$$H_0(-z)L_0(-z) \approx H_0(-z) \quad (3.15)$$

The reconstruction conditions are simplified by these approximations.

$$F_0(z)H_0(z) + F_1(z)H_1(z) \approx 2z^{-l} \quad (3.16)$$

$$F_0(z)H_0(-z) + F_1(z)H_1(-z) \approx 0 \quad (3.17)$$

$$|F_1(z)E_G| = \epsilon \quad (3.18)$$

When equality holds for (3.16) and (3.17), the perfect reconstruction conditions of a conventional two-channel filter bank [20] are met. For any perfect reconstruction filter bank, the output is simplified to:

$$\tilde{A}(z) \;=\; z^{-l}B(z) - \frac{1}{2}F_1(z)E_G \tag{3.19}$$

An $\tilde{A}(z)$ that closely resembles the signal $B(z)$ with a small error factor E_G is produced. E_G changes spatially. Regions where the two images have high edge correlation are locations where the algorithm will perform well.

3.2 Analysis of Error

As stated in the beginning of Chapter 3, $H_0(z)$ is required by the derivation to have a lower transition frequency than $L_0(z)$. The approximations (3.14) and (3.15) are true under this assumption. For a two-channel perfect reconstruction filter bank, H_0 has a transition band centered at $\omega = 0.5\pi$ [20]. $L_0(z)$ transition frequency is determined by the system, This frequency may be less than 0.5π. Levels of sub-band decomposition are added to the system in order to avoid this conflict.

For this problem, traditional optimization techniques cannot be applied to a rigorous mathematical system model. Instead, the system is simplified to the special case of modeling the lens as a low-pass filter on the blue color plane. A large number of experiments and simulations was run in order to recover the high frequency spectra of the original signal. Poor results are produced by conventional methods. For the proposed algorithm, this part of the spectrum is replaced with the corresponding green sub-bands.

As discussed in beginning of Chapter 3, high frequency blue sub-bands are filtered out, but high frequency green sub-bands are passed on. There exists a trade-off between the error created by using the green sub-bands versus the error created by the lens when blurring the blue sub-bands. For this algorithm, when the frequencies of the blue sub-band are not passed by the lens, the green sub-bands are favored by the trade-off. Shown in Section 3.2, the level of decomposition, c,

is increased until the transition frequency of the blurring filter falls beyond the transition frequency of the lowest sub-band.

Determining the Levels of Decomposition

Recall that the blur filter of the blue image is represented by $L_0(e^{j\omega})$. The approximate frequency response is considered:

$$L_0(e^{j\omega}) \approx \left\{ \begin{array}{ll} 1 & \text{if } |\omega| < \pi/4 \\ 0 & \text{if } \pi/4 \leq |\omega| < \pi \end{array} \right\} \tag{3.20}$$

The blue sub-bands are used for all frequencies $|\omega| < \pi/4$ that the lens passes. The green sub-bands are used for all frequencies $\pi/4 \leq |\omega| < \pi$. For this $L_0(e^{j\omega})$, a two-level decomposition is required. In Fig. 3.2, a two-level decomposition for a one dimensional signal is shown:

$$\begin{aligned} \widehat{BLL}(z) &= \frac{1}{2}[H_0(z^{1/2})\frac{1}{2}(H_0(z^{1/4})\hat{B}(z^{1/4}) \\ &\quad +(H_0(-z^{1/4})\hat{B}(-z^{1/4})))] \\ &\quad +\frac{1}{2}[H_0(-z^{1/2})\frac{1}{2}(H_0(jz^{1/4})\hat{B}(jz^{1/4}) \\ &\quad +(H_0(-jz^{1/4})\hat{B}(-jz^{1/4})))] \end{aligned} \tag{3.21}$$

The $\widehat{BLH}$, $\widehat{BHL}$, and $\widehat{BHH}$ terms of the algorithm are replaced with their respective $\widehat{GLH}$, $\widehat{GHL}$, and $\widehat{GHH}$ terms. The original B signal are estimated poorly by the $\widehat{BLH}$, $\widehat{BHL}$, and $\widehat{BHH}$ sub-bands. The accuracy of our estimate of these sub-bands is dependent on the reconstruction error. The original B signal is estimated well by the unfiltered sub-bands of $\widehat{GLH}$, $\widehat{GHL}$, and $\widehat{GHH}$ because of strong edge correlation.

The following change of variables is considered:

$$R(z) = H_0(z)[B(z) - \hat{B}(z)] \tag{3.22}$$

$$P(z) = H_0(z)B(z)(1 - L_0(z)) \tag{3.23}$$

The error between BLL and $\widehat{BLL}$ is represented by E_{BLL}:

$$\begin{aligned} E_{BLL}(z) &= BLL(z) - \widehat{BLL}(z) && (3.24) \\ &= \frac{1}{4}[H_0(z^{1/2})R(z^{1/4})] \\ &\quad + \frac{1}{4}[H_0(z^{1/2})R(-z^{1/4})] \\ &\quad + \frac{1}{4}[H_0(-z^{1/2})R(jz^{1/4})] \\ &\quad + \frac{1}{4}[H_0(-z^{1/2})R(-jz^{1/4})] && (3.25) \\ &= \frac{1}{4}[H_0(z^{1/2})P(z^{1/4})] \\ &\quad + \frac{1}{4}[H_0(z^{1/2})P(-z^{1/4})] \\ &\quad + \frac{1}{4}[H_0(-z^{1/2})P(jz^{1/4})] \\ &\quad + \frac{1}{4}[H_0(-z^{1/2})P(-jz^{1/4})] && (3.26) \end{aligned}$$

E_{BLL} is comprised of four distinct terms. For the first term, $L_0(e^{j\omega/4}) \approx 1$ when $|\omega| < \pi$, thus this term is ≈ 0. For the second term, H_0 is a low-pass filter. $H_0(-e^{j\omega/4}) \approx 0$ by construction and the second term is ≈ 0. For the remaining two terms, H_0 is a low-pass filter. $H_0(-e^{j\omega/2}) \approx 0$ by construction and those terms are ≈ 0. In order to make E_{BLL} small, H_0 should approximate an ideal low-pass filter as much as possible. By adding more coefficients to our filters, an improvement in performance is expected. Since the frequencies in this sub-band are passed by $L_0(e^{j\omega/4})$, a small error E_{BLL} is produced by this estimate.

Consider generalizing L_0:

$$L_0(e^{j\omega}) \approx \left\{ \begin{array}{ll} 1 & \text{if } |\omega| < \omega_0 \\ 0 & \text{if } \omega_0 < |\omega| < \pi \end{array} \right\} \quad (3.27)$$

In order to reduce the overall error, the algorithm can increase the level c decomposition until $\frac{\pi}{2^c} \leq \omega_0 \leq \frac{\pi}{2^{c-1}}$. Choosing a large c, parts of the frequency spectrum are discarded by the algorithm which the lens does not corrupt. Choosing a small c, the error is increased because in the low band of the frequency spectra $0 \neq 1 - L(z)$.

The $\widehat{BLH}$, $\widehat{BHL}$, and $\widehat{BHH}$ are blurred by the optical properties of the lens. A high approximation error is produced. $\widehat{GLH}$, $\widehat{GHL}$, and $\widehat{GHH}$ are better estimates of the edges of the original blue signal.

$$\begin{aligned} E_{BLH} &= BLH - \widehat{BLH} \\ E_{BHL} &= BHL - \widehat{BHL} \\ E_{BHH} &= BHH - \widehat{BHH} \end{aligned} \tag{3.28}$$

$$\begin{aligned} E_{GLH} &= BLH - \widehat{GLH} \\ E_{GHL} &= BHL - \widehat{GHL} \\ E_{GHH} &= BHH - \widehat{GHH} \end{aligned} \tag{3.29}$$

Here, $|E_{GHH}| \leq |E_{BHH}|$, $|E_{GHL}| \leq |E_{BHL}|$, and $|E_{GLH}| \leq |E_{BLH}|$.

The $\widehat{GLH}$, $\widehat{GHL}$, and $\widehat{GHH}$ terms are passed through the rest of the system. The reconstruction conditions in [20] must be satisfied by the filter bank. The output of the system is shown in the expression below:

$$\begin{aligned} \tilde{A}(z) &= z^{-l}B(z) - F_0(z)F_0(z^2)E_{BLL} \\ &\quad -F_0(z)F_1(z^2)E_{GLH} - F_1(z)F_0(z^2)E_{GHL} \\ &\quad -F_1(z)F_1(z^2)E_{GHH} \end{aligned} \tag{3.30}$$

More E_G terms are produced as the decomposition level is increased. To reduce E_{BLL} without introducing extra E_G terms, the level c is increased until $\frac{\pi}{2^c} \leq \omega_0 \leq \frac{\pi}{2^{c-1}}$.

Designing a Pre-Filter

The number of E_G terms is limited by the algorithm. Only the sub-bands with small E_B terms are used. In Section 3.2 , E_{BLL} had four terms in (3.26). Following the same line of reasoning, the error E_{BLH} between BLH and $\widehat{BLH}$ is considered:

$$
\begin{aligned}
P(z) &= H_0(z)B(z)(1 - L_0(z)) && (3.31)\\
E_{BLH}(z) &= BLH(z) - \widehat{BLH}(z) && (3.32)\\
E_{BLH}(z) &= \frac{1}{4}H_1(z^{1/2})P(z^{1/4}) \\
&\quad + \frac{1}{4}H_1(z^{1/2})P(-z^{1/4}) \\
&\quad + \frac{1}{4}H_1(-z^{1/2})P(jz^{1/4}) \\
&\quad + \frac{1}{4}H_1(-z^{1/2})P(-jz^{1/4}) && (3.33)
\end{aligned}
$$

Similar to (3.26), (3.33) has four terms. The first three terms are ≈ 0 by construction because $H_1(e^{j\omega/2}) \approx 0$ and $H_0(je^{j\omega/4}) \approx 0$. However, error is contained in the last term.

To reduce this error, $\widehat{BLH}$ is replaced with the highly correlated $\widehat{GLH}$. For the lower frequency sub-bands, the correlation is poor and errors are seen in the reconstruction. To reduce the error further, before placing the image through the filter bank, pre-filter $W_0(z)$ is added directly after $L_0(z)$. By adding this filter, the fourth term of (3.33) changes:

$$\frac{1}{4}Q(-jz^{1/4})[1 - L_0(-jz^{1/4})W_0(-jz^{1/4})] \tag{3.34}$$

Here, $Q(z) = H_1(z^2)H_0(z)B(z)$.

To make the last term approximately zero, a filter $W_0(z)$ is designed that satisfies the following condition:

$$1 - L_0(-jz^{1/4})W_0(-jz^{1/4}) = 0 \tag{3.35}$$

Assume that more about $L_0(e^{j\omega})$ is known.

$$L_0(e^{j\omega}) \approx \left\{ \begin{array}{ll} 1 & \text{if } |\omega| < \omega_0 \\ \delta & \text{if } \omega_0 < |\omega| < \omega_\delta \\ 0 & \text{if } \omega_\delta < |\omega| < \pi \end{array} \right\} \tag{3.36}$$

$0 < \delta < 1$ and represents the transition band. The first zero of $L_0(e^{j\omega})$ has a higher frequency than ω_δ. A modified Wiener filter can be designed [9] to reduce the error

in all sub-bands with frequencies below ω_δ. Through testing, the regularization problems associated with Wiener filtering were found to occur when $\delta < 0.1$.

$$W_0(e^{j\omega}) \approx \left\{ \begin{array}{rl} \frac{1}{L_0(e^{j\omega})} & \text{if } |\omega| < \omega_\delta \\ 0 & \text{if } \omega_\delta \leq |\omega| < \pi \end{array} \right\} \tag{3.37}$$

The E_B terms for these lower sub-bands are reduced by the W_0 pre-filter. During reconstruction, all $\hat{B}$ sub-bands are used when the frequencies is less than ω_δ. The level of decomposition is increased by the filter bank design so that the highest $\hat{B}$ sub-band used in reconstruction has a transition frequency that is arbitrarily close to ω_δ. In practice, the number of levels of decomposition is limited by complexity and image size issues.

3.3 Experimental Results

3.3.1 Results without Pre-filtering

In Fig. 3.6, the blue image of *Barbara* is shown. The blue color plane is blurred with a 10x10 Gaussian kernel with a standard deviation (STD) of 5. Poisson noise is added to the image after blurring. In Fig. 3.6(d), the results are shown of a four-level decomposition from modified code in [40] without any additional pre-filtering. The reconstruction does well on the high edge correlation between color planes of the table cloth. Compared to the Lucy-Richardson deconvolution results, significant improvement is seen in the results of the proposed method.[1]

To illustrate possible artifacts of the method described in Section 3.2, another example image is shown in Fig. 3.7. At the center of the blue image (Fig. 3.7(a)), the dark object is shown with a light background. For the green image (Fig. 3.7(b)), the light object is shown with a light background. The assumption of strong edge correlation is no longer valid, a poor reconstruction with color bleeding is produced (Fig. 3.7(b)).

[1]More simulation results including video are available at: http://videoprocessing.ucsd.edu/∼jack865/IEEETranColor/

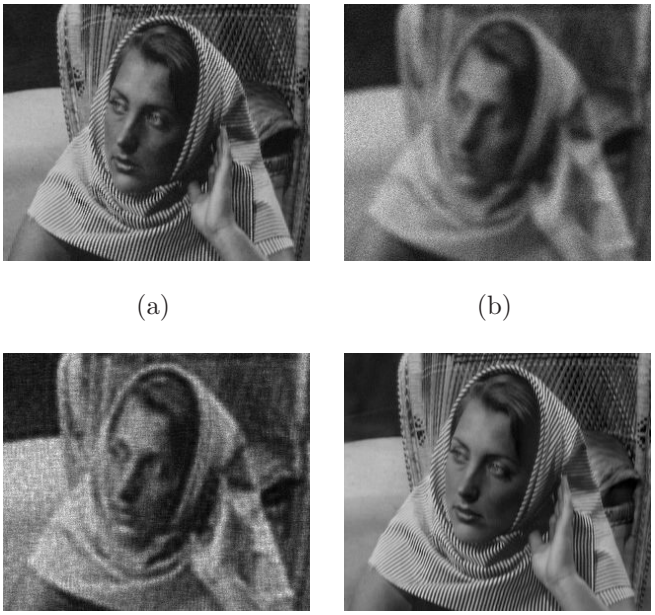

(a) (b)

(c) (d)

Figure 3.6: This test simulates blur using a Gaussian blur kernel. The proposed image has sharper edges than the Lucy-Richardson deconvolution image. (a) Original image; (b) blurred and noisy image; (c) Lucy-Richardson deconvolution; (d) proposed algorithm.

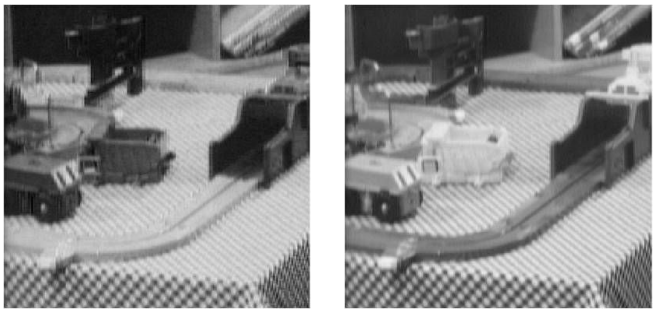

(a) (b)

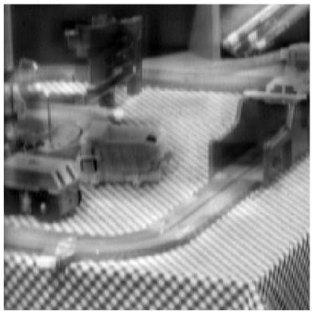

(c)

Figure 3.7: Poor edge correlation between the original blue and green images can lead to color bleeding during reconstruction. (a) Original blue image; (b) original green image; (c) reconstructed blue image.

By sharing information in the reconstructed color image, a sharp color edge is produced by the green image and the blue image. In Fig. 3.8(a), the original color image is shown. In Fig. 3.8(b), the blurred blue image has reduced edge quality and a yellow tint. In Fig. 3.8(c), the proposed method is visually closer to Fig. 3.8(a).

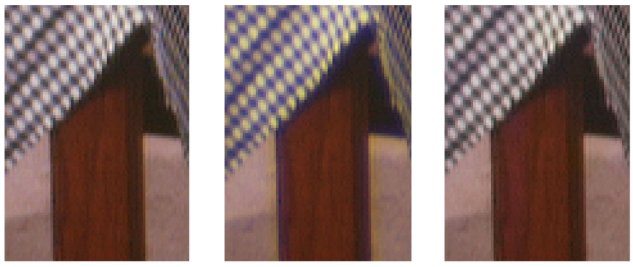

(a) (b) (c)

Figure 3.8: Color images show that the proposed algorithm removes a yellowish tint that appears in the blurred color image. (a) Original image; (b) blurred image; (c) proposed image.

In Fig. 3.9, the PSNR results of the proposed algorithm are compared with conventional Wiener deconvolution method when the standard deviation of a Gaussian kernel is increased for a fixed window size and Additive White Gaussian Noise (AWGN) with standard deviation 0.05 has been added. For all other graphs in this chapter, noise is not added to the system. In Chapter 4 and Chapter 6, AWGN and Poisson noise are more fully explored.

The proposed method without a pre-filter has PSNR values approximately 5 dB higher than traditional methods for different blur kernels. Listed as PR, the proposed algorithm uses different wavelets. As the number of filter coefficients increases, the Daubechies wavelets [19] have slightly improved results. This observation matches the derivation in Section 3.2. Comparable results to the Daubechies filters are produced by the Farras nearly symmetric orthogonal filters [40].

In Fig. 3.10, the PSNR results are shown of different levels of decomposition when the standard deviation for the blur kernel is fixed, and the kernel size is increased. At smaller kernel sizes, the best result is produced by a three-level decomposition. However as the size of the kernel increases, the best PSNR is

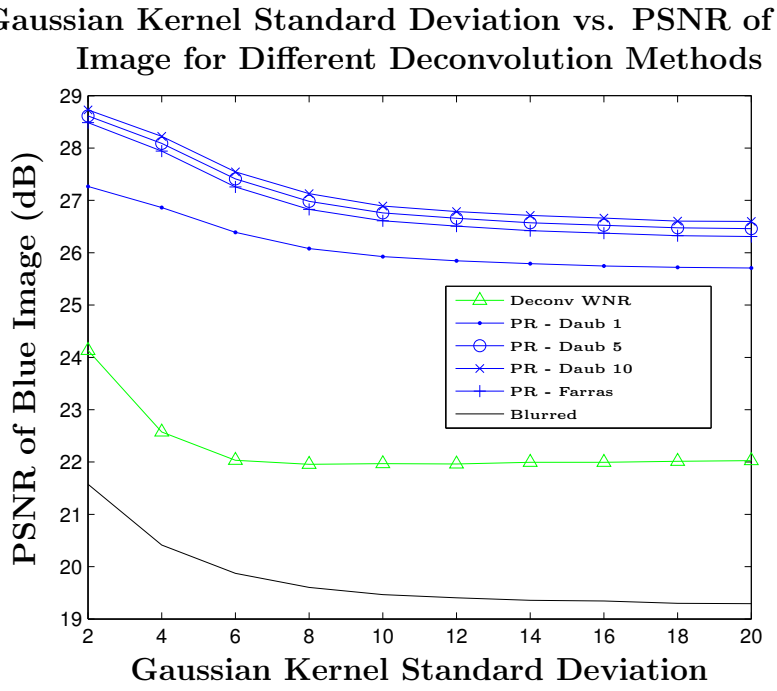

Figure 3.9: Different deconvolution methods to the proposed (noted as PR) method are compared in this simulation when using a fixed 21x21 window. The proposed method performs 5 dB better than the Wiener method.

produced by higher levels of decomposition. The four-level decomposition curve has three regions: kernel size 5 to 12 when the three-level decomposition has the highest PSNR, kernel size 13 to 22 when the four-level decomposition has the highest PSNR, and kernel size 23 to 50 where five and six-level decomposition have the highest PSNR.

In region one, $\omega_0 \geq \frac{\pi}{2^3}$. Uncorrupted information is discarded by the four-level decomposition and additional E_G terms are added. In this region the best performance is seen with less than 4 levels. A flat slop is seen for the 4 level curve. The minor incremental effect that the E_G terms have is indicated by this flat slope.

In region two, $\frac{\pi}{2^3} \geq \omega_0 \geq \frac{\pi}{2^4}$. The highest PSNR is produced by the four-level decomposition. In this region, all the information that the lens has not blurred is used and extra E_G terms are not present.

In region three, $\frac{\pi}{2^4} \geq \omega_0$. Blurred parts of the frequency spectrum are used by the four-level decomposition. $L_0 < 1$ for portions of the low frequency sub-band. The original assumption is broken and E_{BLL} is increased. A larger level

of decomposition is needed. A steep slope is seen in the four-level decomposition curve in this region. The major effect that an increase in the E_{BLL} term has on the reconstruction error is indicated by this observation. A larger penalty is suggested by the model and the simulation results when the algorithm uses a small level of decomposition.

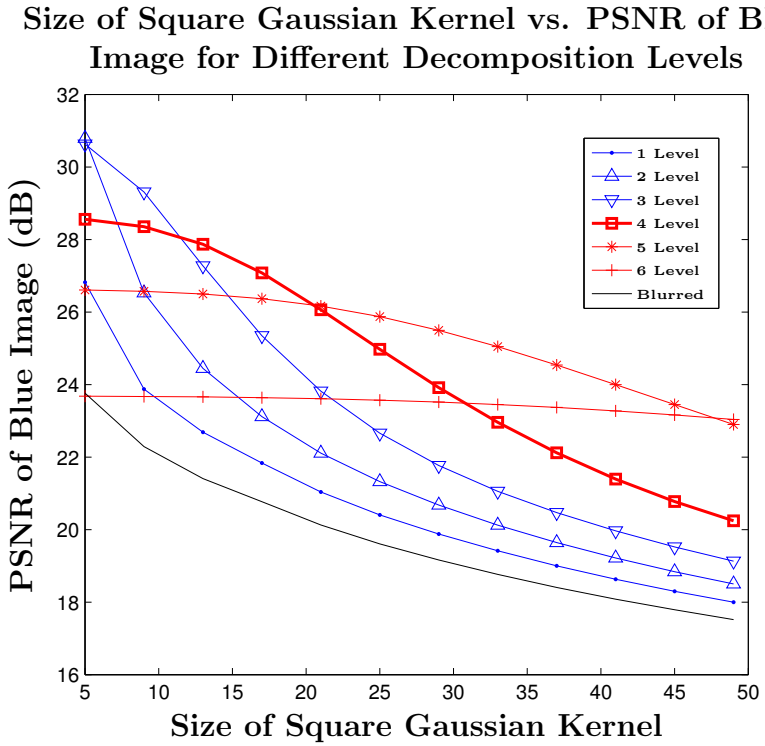

Figure 3.10: The relationship between kernel size and decomposition level are tested in this simulation. A fixed standard deviation at 50 and a Daubechies 5 tap filter are used in this simulation.

In Fig. 3.11, the PSNR results are shown of different levels of decomposition with a window size for the blur kernel that is fixed and a standard deviation that is increasing. As the standard deviation is increased, the best PSNR value is produced by a higher level of decomposition. For a six-level decomposition, the PSNR does not change with respect to the standard deviation. The image is down-sampled several times. Changing the standard deviation has little effect on the resulting reconstruction. A better result is produced by the six-level decomposition than the results of the one or two-level decomposition. A small penalty for using too high a level is indicated by these results. A large penalty for using too small

a level is also indicated.

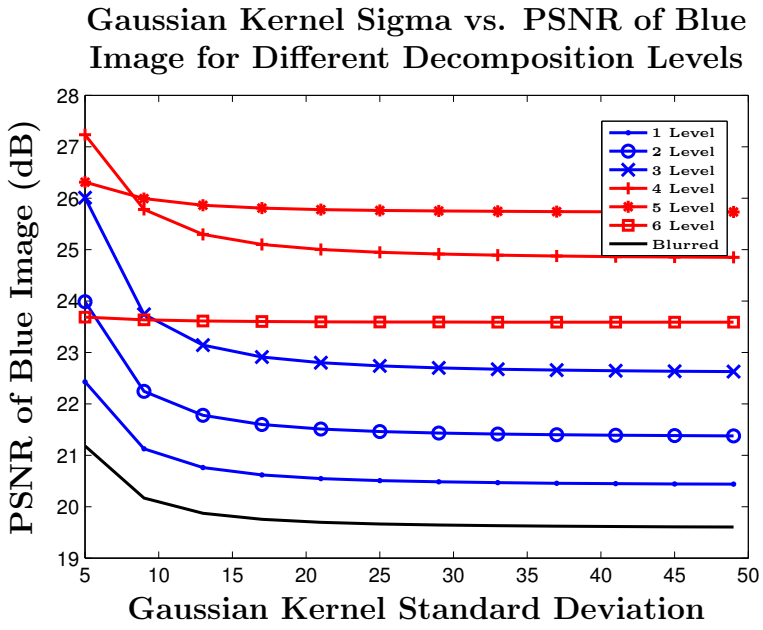

Figure 3.11: The relationship between standard deviation of Gaussian kernel and level of decomposition are shown. A fixed 25x25 window with a Daubechies 5 tap filter is used by this simulation.

3.3.2 Simulation on Different Wavelets

In Fig. 3.12, the results are shown of different wavelet filters on a synthetic image. In Fig. 3.12(a) and Fig. 3.12(b), the effects of different correlation values between the edges of the blue and green images are highlighted. An extremely poor edge correlation case is shown in the middle and top portions of the images. A high edge correlation case is shown in the bottom portions of the images. Fixing the number of filter coefficients, the results of the Daubechies 5, Symlets 5, Biorthogonal 2-4 and Biorthgonal 4-4 wavelets [19] are shown in Fig. 3.12(c) to Fig. 3.12(f). For the high edge correlation case, good results are produced by all reconstructions. The correct shading level is maintained throughout most of the image. For the poor edge correlation case, poor results are produced by the reconstructions.

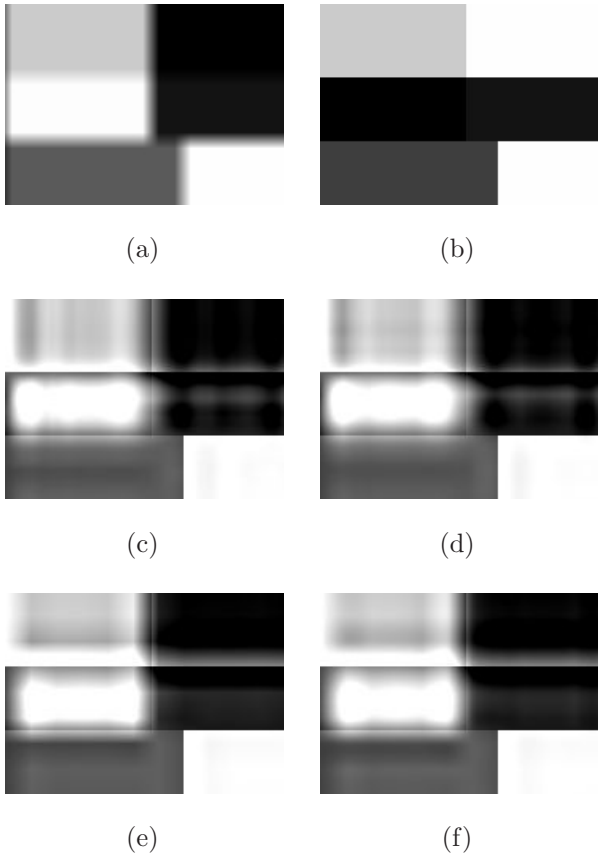

(a) (b)

(c) (d)

(e) (f)

Figure 3.12: Reconstruction results of different wavelets are compared by this synthetic image test when using a fixed number of filter coefficients. The cases of both strong and weak edge correlation between the blue and green images are shown in this test. (a) Blurred blue image; (b) green image; (c) Daubechiews 5; (d) Symlets 5; (e) Biorthogonal 2-4; (f) Biorthogonal 4-4.

3.3.3 Simulation Results with Pre-filtering

The pre-filter $W_0(z)$ is used to recover a piece of the lower frequency band directly from the blurred blue image. However, ω_δ of the blurring filter is needed. At frequencies higher than ω_δ, the green image sub-bands are favored by the trade-off.

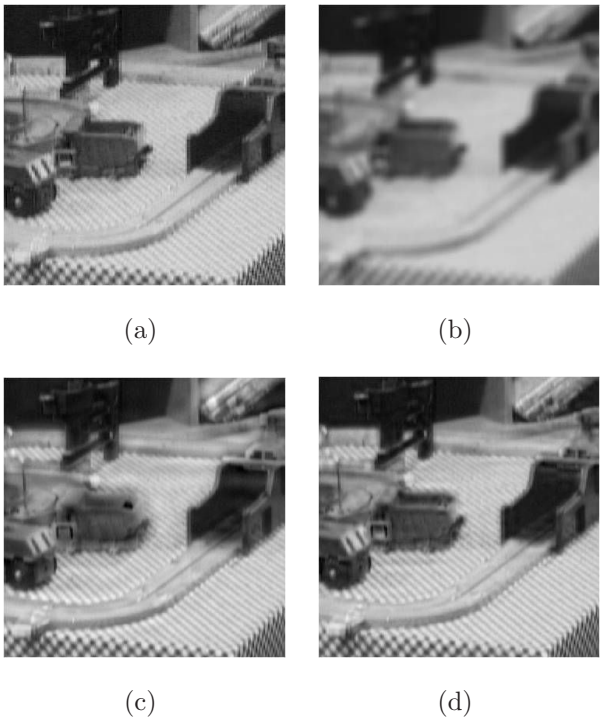

(a) (b)

(c) (d)

Figure 3.13: A reconstruction which more closely resembles the original image is produced by the addition of a pre-filter. (a) Original image; (b) blurred image; (c) proposed image without pre-filtering; (d) proposed image with pre-filtering.

In Fig. 3.13, the effects of pre-filtering are demonstrated. In Fig. 3.13(c), without the pre-filtering, smudged edges in the reconstructed image are the result of the poor correlation between green and blue in this area. However, this poor correlation is overcome by the addition of pre-filtering in 3.13(d). In 3.13(d), the problem of smudging of color is no longer present.

In Fig. 3.14, the best results are compared from the proposed algorithm with and without pre-filtering. The same simulation from Fig. 3.10 is repeated using a pre-filter. Only the best PSNR results among all the levels of decomposition

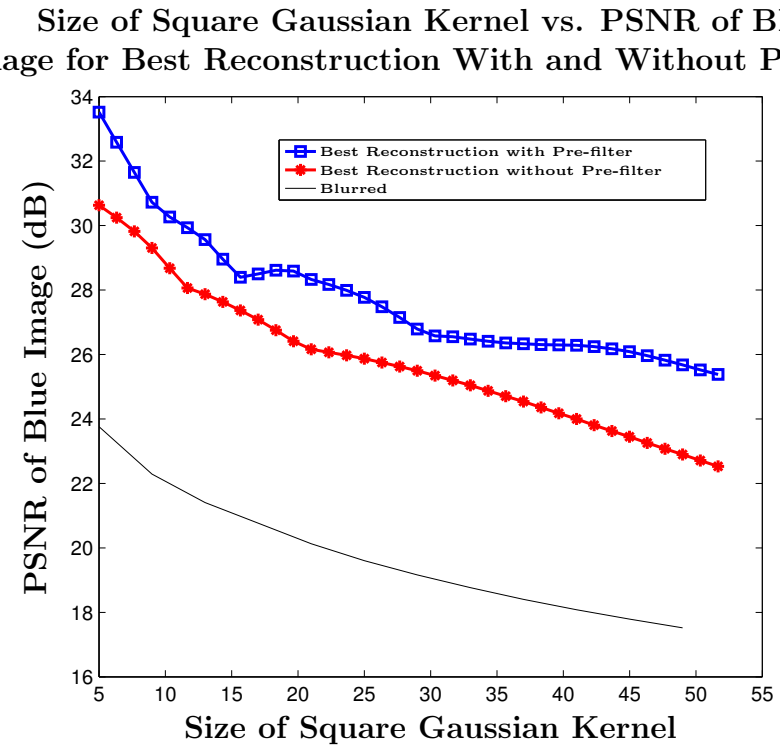

Figure 3.14: The effectiveness of additional pre-filtering is tested in this simulation. A fixed standard deviation at 50 is used in this simulation.

are shown.

Initially, a 3 dB higher PSNR is produced by this simulation. Looking at (3.36) for this region, the ω_0 point of L_0 has a much lower frequency than the ω_δ point. Without pre-filtering, the frequency sub-bands of the blue image between ω_0 and ω_δ are replaced with sub-bands from the green image. With pre-filtering, the low frequency blue image sub-bands are used and fewer E_G terms are produced.

When the kernel size is 9, 16, and 32, approximately 1 dB of gain is produced by pre-filtering. In these regions, the same number of sub-bands is used by both algorithms. The same number of E_G terms is contained. A smaller difference in PSNR is produced by this effect. 8-10 dB higher performance than the blurred image is produced by the proposed algorithm with a pre-filter.

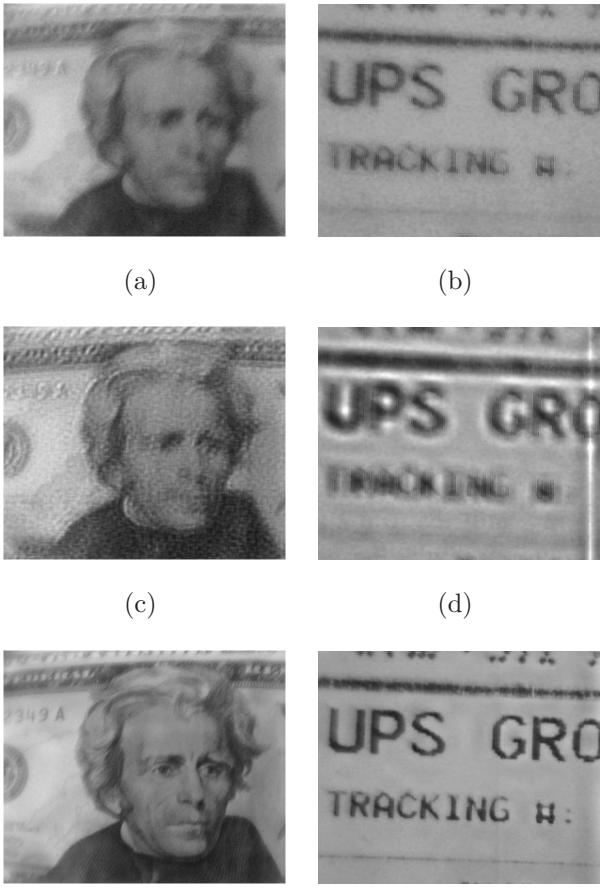

Figure 3.15: This image shows actual images taken from the device with blur caused by the FLCS. This experiment compares the proposed algorithm to the Lucy-Richardson algorithm. (a) Actual blue image; (b) actual blue image; (c) Lucy-Richardson algorithm; (d) Lucy-Richardson algorithm; (e) proposed algorithm; (f) proposed algorithm.

3.3.4 Actual Images Taken from the Device

In Section 3.3.1 simulated blur kernels were used. In Fig. 3.15, actual images were used from the device. In Fig. 3.15(a) and Fig. 3.15(b), actual lens blur and not simulated blur is shown. The images taken were from a distance of 15 cm from the lens in a well lit laboratory setting. Additional information about the test conditions and lens functionality can be found in [1]. For this test, the lens parameters are set to maximize the quality of the green color plane at the expense of the other color planes. By adjusting these parameters, the FLCS is tuned to favor an alternate color plane at the expense of the remaining two.

In Fig. 3.15, the results of the Lucy-Richardson algorithm are compared to the proposed algorithm. The Lucy-Richardson method has a problem with over sharpening (Fig. 3.15(c)). This problem is mitigated by the proposed algorithm. The shading layer is preserved by the blue image. The green image edges of the reconstruction are improved (Fig. 3.15(e) and Fig. 3.15(f)). The blur artifacts caused by the lens are reduced and the results are sharpened.

The text of Chapter 3 is adapted from *Image Enhancement for Fluid Lens Camera Based on Color Correlation*, Jack Tzeng and Truong Nguyen, in the February 2009 issue of *IEEE Transactions on Image Processing*. The dissertation author was the primary author of these publications, and the co-author listed directed and supervised the research which forms the basis for this chapter.

Chapter 4

Contourlet Sub-band Meshing

In Chapter 3, the Wavelet Sub-band Meshing algorithm is proposed to deal with the non-uniform color blurring of the FLCS. When the edges between the green and blue color planes match, a large increase in sharpness is seen in the reconstructed images. However, when the edges do not match, color bleeding artifacts are seen in the image. Smudged edges are produced by these color bleeding artifacts.

Compared to the wavelet transform [20, 19], images containing contours and textures are better represented by the contourlet transform [17, 18]. A Laplacian pyramid and a directional filter bank are used to produce a multi-scale image with several directional sub-bands. The contour information is represented efficiently by this directional filter bank. The wavelet transform does not have a directional filter bank. The natural contours of the image are preserved by the contourlet transform.

The Contourlet Sub-band Meshing algorithm is an attempt to reduce the color bleeding artifacts. Similar to the wavelet-based method, a complicated PSF estimation is not required. The smudging and ghosting artifacts produced by the wavelet-based method are reduced by this directional filter bank approach. In areas where the green and blue color planes have similar edges, this method performs as well as the Wavelet Sub-band Meshing algorithm. In areas where the green and blue color planes do not have similar edges, these color bleeding artifacts are reduced using the Contourlet Sub-band Meshing algorithm.

4.1 The Algorithm

For the Contourlet Sub-band Meshing algorithm, the same basic framework as the Wavelet Sub-band Meshing algorithm is followed. A directional contourlet filter bank is used to extract edge information from the green image. Fewer ghosting artifacts than the wavelet-based algorithm are produced.

1. A contourlet filter bank is selected and the images are decomposed into sub-bands by filtering and down-sampling.

2. As the size of the PSF increases, the blue image will become more blurry with fewer sharp edges. More levels of decomposition are introduced by further down-sampling and filtering the lowest frequency sub-band.

3. The green contourlet coefficients for the higher sub-bands are selected to replace the corresponding blue sub-bands.

4. In the lowest sub-band, the original blurred blue color sub-band is kept in order to reduce false coloring.

5. Reconstruction is performed by up-sampling and filtering.

4.2 Analysis of the algorithm

4.2.1 Mean Squared Error of Contourlet Sub-band Meshing

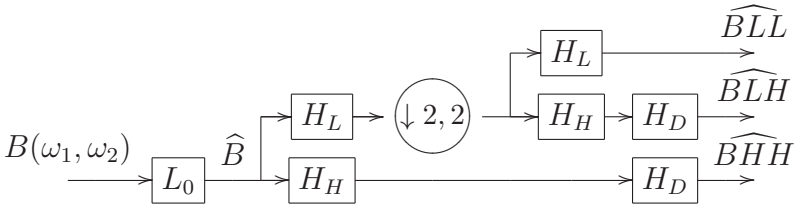

Figure 4.1: A 2-D Contourlet Filter Bank.

In Fig. 4.1, the basic contourlet transform [18] is shown where L_0 represents the lens blur. All filters are assumed to have unity gain at DC. Reducing the MSE

between the result and the clean blue image, $B(\omega_1, \omega_2)$ is the goal of this algorithm. Compared to the wavelet based algorithm, the contourlet coefficients are able to adjust to the natural contours of the image. A more natural looking image is produced during reconstruction.

Fig. 4.1 has three outputs: the low-pass output $\widehat{BLL}$, the band-pass output $\widehat{BLH}$, and the high-pass output $\widehat{BHH}$. The respective $\widehat{GLH}$ and $\widehat{GHH}$ are substituted into the algorithm. The conditions under which the proposed algorithm better estimates $B(\omega_1, \omega_2)$ and reduces the MSE are discussed.

Consider $\widehat{BLH}$ expressed in terms of $B(\omega_1, \omega_2)$.

$$\begin{aligned}\widehat{BLH} &= 0.25H_D(\omega_1,\omega_2)H_H(\omega_1,\omega_2)[\sum_{m=0}^{1}\sum_{n=0}^{1} \\ &\quad H_L(\frac{\omega_1}{2}+n\pi,\frac{\omega_2}{2}+m\pi)L_0(\frac{\omega_1}{2}+n\pi,\frac{\omega_2}{2}+m\pi) \\ &\quad B(\frac{\omega_1}{2}+n\pi,\frac{\omega_2}{2}+m\pi)] \end{aligned} \tag{4.1}$$

H_L is a low-pass filter, H_H is a high-pass filter, and H_D is a group of directional filters. The first order term is the $m = 0, n = 0$ term. All other values are close to 0 and produce second or third order terms. The focus of this analysis is centered around the $m = 0, n = 0$ term. Similar BLH and $\widehat{GLH}$ terms are created by the clean blue image and the green image.

The $\widehat{GLH}$ is used when it produces a smaller MSE.

$$|BLH - \widehat{GLH}|^2 < |BLH - \widehat{BLH}|^2 \tag{4.2}$$

In this case, the $|BLH - \widehat{BLH}|^2$ term is the error in the reconstruction when the algorithm uses the original blurred blue sub-band. The $|BLH - \widehat{GLH}|^2$ term is the error in the reconstruction when the green sub-band is extracted and is substituted into the system. For this approach to be effective, the MSE of this term must be lower than the MSE of the other term.

Many of the similar terms are combined into variable a:

$$a = 0.25H_D(\omega_1,\omega_2)H_H(\omega_1,\omega_2)H_L(\frac{\omega_1}{2},\frac{\omega_2}{2}) \tag{4.3}$$

$$\begin{aligned} &a^2[B(\frac{\omega_1}{2},\frac{\omega_2}{2}) - \widehat{G}(\frac{\omega_1}{2},\frac{\omega_2}{2})]^2 \\ &< a^2[B(\frac{\omega_1}{2},\frac{\omega_2}{2}) - L_0(\frac{\omega_1}{2},\frac{\omega_2}{2})B(\frac{\omega_1}{2},\frac{\omega_2}{2})]^2 \end{aligned} \tag{4.4}$$

The following equation is produced by removing $a^2 B(\frac{\omega_1}{2}, \frac{\omega_2}{2})^2$ from both sides:

$$[1 - \frac{\widehat{G}(\frac{\omega_1}{2}, \frac{\omega_2}{2})}{B(\frac{\omega_1}{2}, \frac{\omega_2}{2})}]^2 < [1 - L_0(\frac{\omega_1}{2}, \frac{\omega_2}{2})]^2 \tag{4.5}$$

$$0 < [1 - L_0(\frac{\omega_1}{2}, \frac{\omega_2}{2})]^2 - [1 - \frac{\widehat{G}(\frac{\omega_1}{2}, \frac{\omega_2}{2})}{B(\frac{\omega_1}{2}, \frac{\omega_2}{2})}]^2 \tag{4.6}$$

The following inequality is produced by a difference of squares:

$$\begin{aligned} 0 < [&\frac{\widehat{G}(\frac{\omega_1}{2}, \frac{\omega_2}{2})}{B(\frac{\omega_1}{2}, \frac{\omega_2}{2})} - L_0(\frac{\omega_1}{2}, \frac{\omega_2}{2})][2 \\ &- L_0(\frac{\omega_1}{2}, \frac{\omega_2}{2}) - \frac{\widehat{G}(\frac{\omega_1}{2}, \frac{\omega_2}{2})}{B(\frac{\omega_1}{2}, \frac{\omega_2}{2})}] \end{aligned} \tag{4.7}$$

Two conditions are created:

$$L_0(\frac{\omega_1}{2}, \frac{\omega_2}{2}) < \min[\frac{\widehat{G}(\frac{\omega_1}{2}, \frac{\omega_2}{2})}{B(\frac{\omega_1}{2}, \frac{\omega_2}{2})},\ 2 - \frac{\widehat{G}(\frac{\omega_1}{2}, \frac{\omega_2}{2})}{B(\frac{\omega_1}{2}, \frac{\omega_2}{2})}] \tag{4.8}$$

$$L_0(\frac{\omega_1}{2}, \frac{\omega_2}{2}) > \max[\frac{\widehat{G}(\frac{\omega_1}{2}, \frac{\omega_2}{2})}{B(\frac{\omega_1}{2}, \frac{\omega_2}{2})},\ 2 - \frac{\widehat{G}(\frac{\omega_1}{2}, \frac{\omega_2}{2})}{B(\frac{\omega_1}{2}, \frac{\omega_2}{2})}] \tag{4.9}$$

If the system satisfies either (4.8) or (4.9), then a better MSE is achieved by the proposed system. By construction, the camera produces a blurred blue image, $L_0(\frac{\omega_1}{2}, \frac{\omega_2}{2}) B(\frac{\omega_1}{2}, \frac{\omega_2}{2}) = \widehat{B}(\frac{\omega_1}{2}, \frac{\omega_2}{2})$. These two conditions are rewritten as the following equations:

$$\begin{aligned} \widehat{B}(\frac{\omega_1}{2}, \frac{\omega_2}{2}) \ &< \ \min[\widehat{G}(\frac{\omega_1}{2}, \frac{\omega_2}{2}), \\ &\quad\ 2B(\frac{\omega_1}{2}, \frac{\omega_2}{2}) - \widehat{G}(\frac{\omega_1}{2}, \frac{\omega_2}{2})] \end{aligned} \tag{4.10}$$

$$\begin{aligned} \widehat{B}(\frac{\omega_1}{2}, \frac{\omega_2}{2}) \ &> \ \max[\widehat{G}(\frac{\omega_1}{2}, \frac{\omega_2}{2}), \\ &\quad\ 2B(\frac{\omega_1}{2}, \frac{\omega_2}{2}) - \widehat{G}(\frac{\omega_1}{2}, \frac{\omega_2}{2})] \end{aligned} \tag{4.11}$$

Conditions similar to (4.8), (4.9), (4.10), and (4.11) can be produced for each of the outputs in Fig. 4.1. In the high frequency sub-bands, $L_0(\frac{\omega_1}{2}, \frac{\omega_2}{2}) \approx 0$ and these coefficients are blurred out by the lens. $x \approx y$ means that $|x - y| < 2^{-10}$. Under these conditions, (4.8) becomes the following inequality:

$$0 < \frac{\widehat{G}(\frac{\omega_1}{2}, \frac{\omega_2}{2})}{B(\frac{\omega_1}{2}, \frac{\omega_2}{2})} < 2 \tag{4.12}$$

For natural images, the magnitudes of the higher frequency components are typically within a factor of 2. Under this condition, the upper bound is satisfied by $\widehat{G}(\frac{\omega_1}{2}, \frac{\omega_2}{2})$ and $B(\frac{\omega_1}{2}, \frac{\omega_2}{2})$. As shown in (4.12), for these high frequency sub-bands, the MSE will be reduced when the green and clean blue coefficients have the same sign and a strong match between the color planes. The condition is not met in areas where they have different signs.

Color bleeding is produced by the poor match. In the green color plane, an edge can go from a dark object to a light background. In the blue color plane, the same edge can go from a light object to a light background. In this instance, the direction of the edges is different. In the color image, yellowish blurred edges are produced by this condition.

For the lowest frequency components, a minor effect on these frequencies is caused by the blur kernel, thus $L_0(\frac{\omega_1}{2}, \frac{\omega_2}{2}) \approx 1$. In this case, $B(\frac{\omega_1}{2}, \frac{\omega_2}{2}) \approx \widehat{B}(\frac{\omega_1}{2}, \frac{\omega_2}{2})$, leaving (4.10) and (4.11) unsatisfied.

4.3 Results

Several results are presented in this section. In Section 4.3.1, the initial sharp image is blurred with a kernel and no noise is added to the system. The deblurring results of the proposed algorithm and wavelet-based algorithm are compared. In Section 4.3.4, real results are presented of images from a prototype of the FLCS in a lab setting. For all tests, in the proposed contourlet algorithm, the Daubechies (db5) [19] filter set is used for the pyramidal structure and PKVA8 filter set developed by Phoong et al. [41, 42] is used as the directional filter. In the wavelet algorithm, the Daubechies (db5) filter set is used. Unless otherwise noted, five levels of decomposition are used.

4.3.1 Noise Free Simulation Results

In Fig. 4.2, the previous wavelet-based method is compared to the proposed method. The blue color plane of a color image is blurred by a 15x15 pixel Gaussian kernel with a standard deviation of 50 and no noise is added. Four levels of

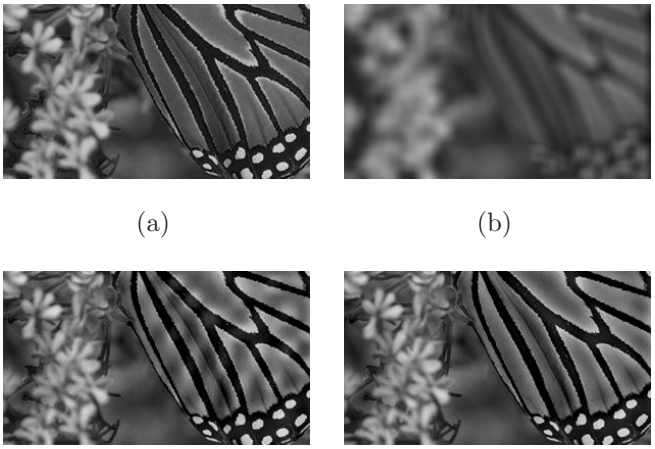

(a) (b)

(c) (d)

Figure 4.2: For these images, the natural boundaries between objects are preserved by the proposed image. (a) Original blue image; (b) blurred image; (c) Wavelet Sub-band Meshing; (d) proposed algorithm.

decomposition are used in both the contourlet-based and wavelet-based methods. Throughout the wing of the butterfly, color bleeding artifacts in Fig. 4.2(c) are caused by ghosting artifacts. In Fig. 4.2(d), the contours of the image are preserved by the proposed algorithm in order to reduce these artifacts and appear closer to the original image.

In Fig. 4.3, the results of processing a color image are shown. In Fig. 4.3(b), the colors are altered and edge details are lost by the blurring of the blue sub-band. For this test, the blue sub-band is blurred by a Gaussian blur kernel of size 5x5 with a standard deviation of 20. For the wavelet-based image, Fig. 4.3(c), smudging that did not appear in the original image is produced by color bleeding in the red oval area. For the proposed contourlet-based image, Fig. 4.3(d), an overall sharper image is produced with fewer false colors and less smudging than the wavelet-based method.

In Fig. 4.4, the proposed algorithm is compared to the wavelet-based algorithm under extreme examples of edge mismatch. The test results are presented for different cases. Areas of high edge matching and areas of low edge matching between the green and blue images are considered. In Fig. 4.4(a) and Fig. 4.4(b), the initial blurred blue and sharp green images are shown. In Fig. 4.4(a), the

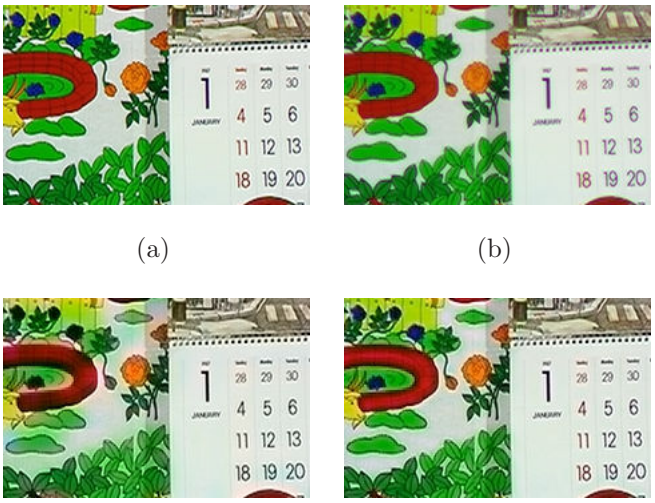

(a) (b)

(c) (d)

Figure 4.3: In the color images, the natural boundaries between objects are preserved and less color bleeding artifacts are seen. The improvement of the proposed algorithm can be seen best in color. (a) Original color image; (b) blurred color image; (c) Wavelet Sub-band Meshing; (d) proposed algorithm.

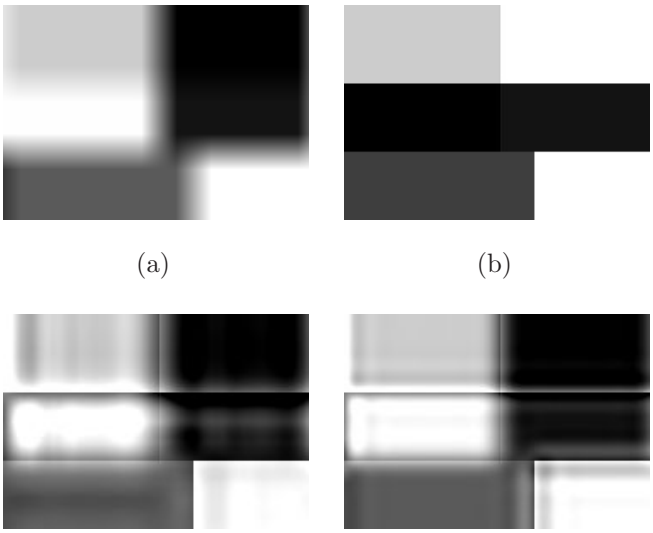

(a) (b)

(c) (d)

Figure 4.4: The results of extreme test cases of strong and weak edge matching between color planes. (a) Blurred blue image; (b) original green image; (c) wavelet; (d) proposed.

blue image has been blurred by a Gaussian window of size 21x21 with a standard deviation of 20. In each of the images, three different degrees of edge matching between blue and green color planes are presented. At the top of Fig. 4.4(a), the transition goes from light to dark, while at the top of Fig. 4.4(b) the transition goes from dark to light. Here, the green and blue edges are in opposite directions. A different case is presented in the middle of the two images. A transition from light to dark is seen in the blue image, while no transition is seen in the green image. Lastly, in the bottom of Fig. 4.4(a) and Fig. 4.4(b), the case when the transitions match is shown.

The wavelet-based method in Fig. 4.4(c) does well in the strongly correlated blocks along the bottom of that image. However, in the areas of weak edge matching, ghosting artifacts and color bleeding problems are suffered by this algorithm. In Fig. 4.4(d), the proposed algorithm is able to align the edges of the image better and to produce a more natural looking result. The original shading levels of the blurred blue image are also maintained.

4.3.2 Noise Added Simulation Results

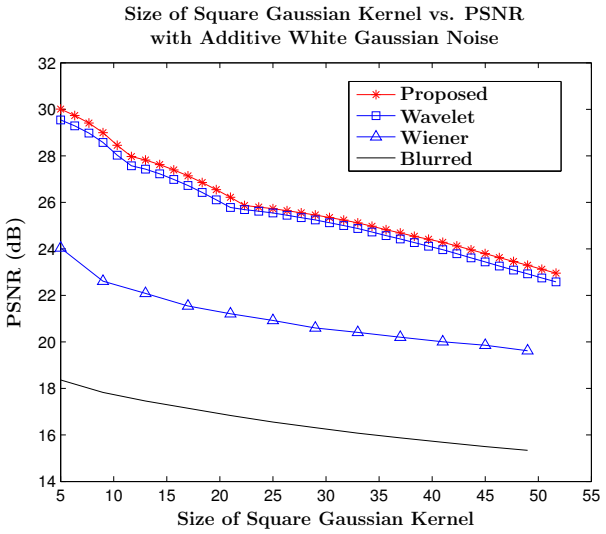

Figure 4.5: The proposed algorithm achieves the highest PSNR.

In the previous experiments, noise is not added to any of the images. In Fig. 4.5, AWGN has been added to the blue channel image after blurring. The goal of

this test is to determine the effects of increasing the size of the blur kernel on each deconvolution algorithm. The standard deviation of the noise is 0.1 and the mean of the noise is 0. The green channel is assumed to be noise free and without blur. The standard deviation of the blur kernel is fixed at 50 while the size of the square blur kernel is increased. For a small kernel, the blurring is a weighted average over a small number of points. For a large kernel, a larger number of points is used. Points on the edge of the blur kernel have a lower weight than points in the center of the kernel. The weights take the shape of a 2-D Gaussian distribution.

The proposed method, wavelet-based method, and Wiener deconvolution method are compared. For the Wiener deconvolution case, the exact PSF used to blur the system is given. The noise autocorrelation matrix and the sharp image autocorrelation matrix are calculated using the noise signal and sharp image signal. These exact values are provided to the Wiener deconvolution to maximize performance. The Lucy-Richardson deconvolution method is not run because a Poisson noise statistic is assumed for that method. With AWGN, the performance of the Wiener deconvolution method is lower than the proposed and wavelet-based methods. The proposed and wavelet-based algorithms rely on edge information from the green channel which does not have noise. For these methods, only the lowest sub-band from the blue image is used. In this sub-band, the noise has zero mean and does not significantly affect performance.

For the proposed algorithm, a higher PSNR over all other algorithms is consistently achieved. Compared to the results from the Wiener deconvolution algorithm, about a 2-3 dB higher PSNR is achieved by the proposed algorithm. Compared to the results from the wavelet-based method, 0.25-0.5 dB higher PSNR is achieved by the proposed algorithm. Although not shown in the graph, as the level of blur is increased, a higher number of decompositions is needed by the algorithm. This effect means that as the blur is increased, more green coefficients are required by the algorithm. False coloring and poor edge matching is increased when more of the green coefficients are used.

While PSNR is used in Fig. 4.5, Structural Similarity (SSIM) is an alternative image quality measure of an output image against a reference original image

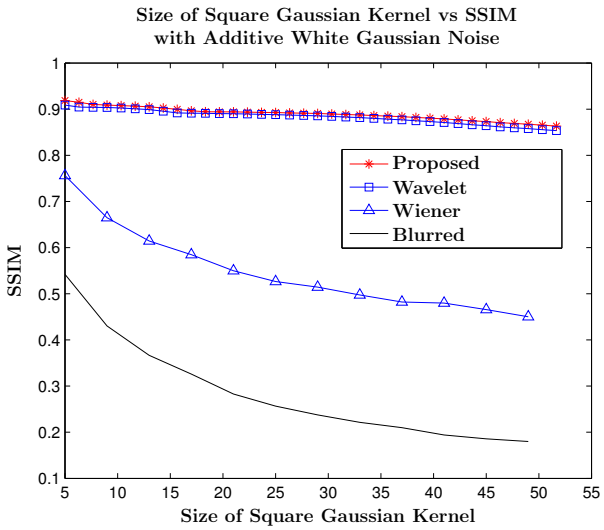

Figure 4.6: The proposed algorithm achieves the highest SSIM.

[43]. The mean and variance of pixel values within a window are compared between the two images. In Fig. 4.6, the same simulation setup is presented as in Fig. 4.5. In both graphs, the highest value is produced by the results of the proposed algorithm. A slightly lower SSIM is achieved by the results of the wavelet-based algorithm. For images produced by the Wiener deconvolution method, the SSIM improvement over the blurred blue image is between 0.2 and 0.3. For images produced by the proposed method, the SSIM improvement over the blurred blue image is between 0.3 and 0.7.

In Fig. 4.7, Poisson noise has been added to the blue channel image after blurring. The green channel is assumed to be noise free and without blur. With Poisson noise, the Lucy-Richardson deconvolution method attempts to achieve the maximum likelihood solution. The exact PSF used to blur the image was used by the algorithm. The algorithm is run for 20 iterations with a damping parameter set at 0.2. The damping parameter of 0.2 was found to achieve the highest PSNR. The Wiener deconvolution method is not run because AWGN is assumed for that method

In Fig. 4.8, the same experiment is run as in Fig. 4.7. Poisson noise is added to the image and the Lucy-Richardson, wavelet-based, and proposed algorithms are used. The SSIM of the outputs are compared. For all values of the kernel

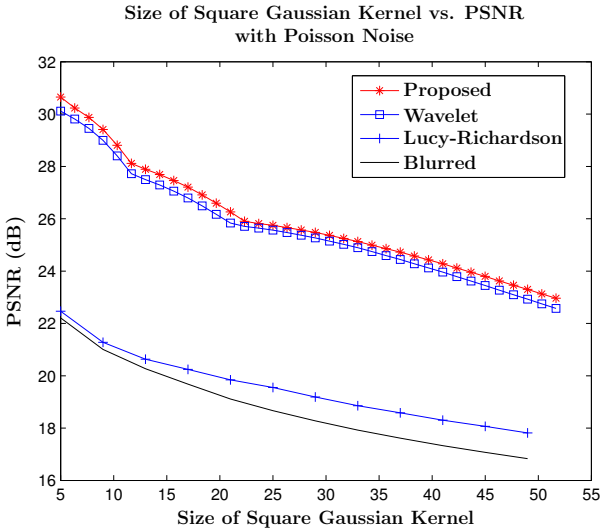

Figure 4.7: The proposed algorithm adjusts to the Poisson noise.

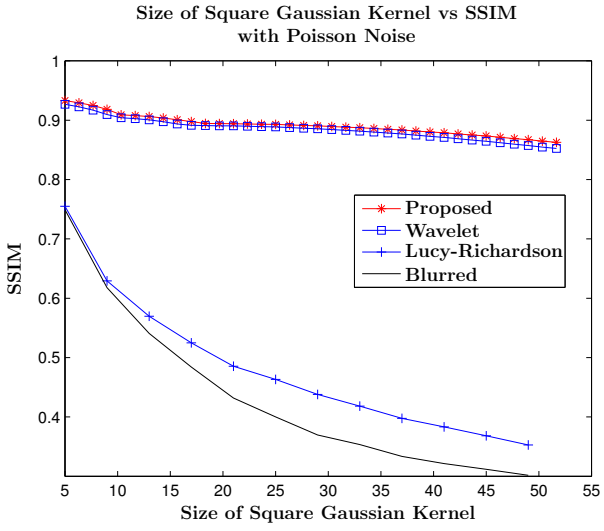

Figure 4.8: The proposed algorithm achieves the highest SSIM.

size, the SSIM is highest for the proposed algorithm and slightly lower for the wavelet-based method. For images produced by the Lucy-Richardson algorithm, a 0-0.1 gain in SSIM over the blurred input is achieved. For images produced by the proposed algorithm, a 0.15-0.55 gain in SSIM over the blurred input is achieved.

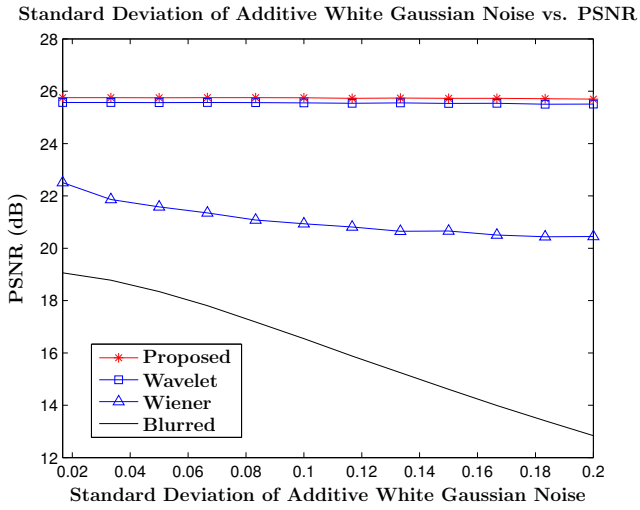

Figure 4.9: The proposed algorithm maintains a stable PSNR.

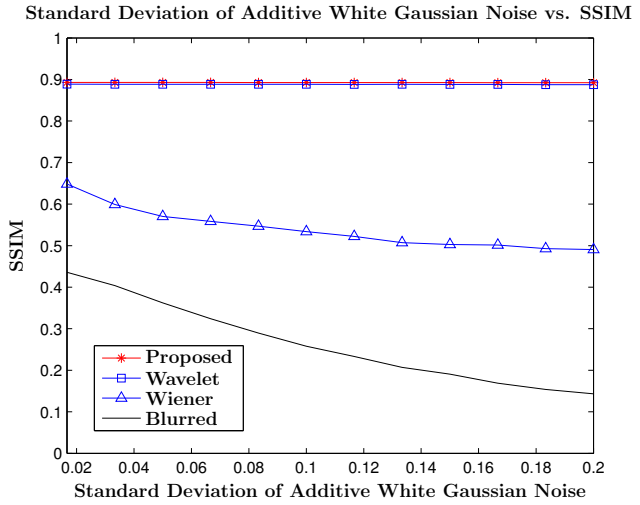

Figure 4.10: The proposed algorithm maintains a stable SSIM.

In Fig. 4.9 and Fig. 4.10, the standard deviation of the AWGN was increased. The goal of this simulation is to understand the effect that AWGN has

on the proposed algorithm. In this experiment, the blue image was blurred by a constant Gaussian Kernel of size 25x25 with standard deviation 50. After blurring, different amounts of AWGN noise were added to the blurred blue image. The standard deviation of the AWGN was increased from 0.02 to 0.2 and the mean is set to 0. The exact PSF and autocorrelation values are provided to the Wiener deconvolution method. As the level of noise is increased, the PSNR and SSIM values of the proposed and wavelet-based methods remain stable. For these algorithms, the green channel which does not have noise is the source of the edge information. The proposed and wavelet-based algorithms only require the lowest sub-band of the blue channel. Noise in this sub-band has only a minor effect on the performance of the proposed algorithm.

4.3.3 Mean Squared Error of Different Domains

In this chapter, the claim is made that more information about the higher frequency components of natural images is contained in the contourlet domain over the color domain. Specifically, less error is produced by a replacement of the contourlet coefficients in the blue color plane with the coefficients in green color plane than a similar replacement of just the blue color pixels with the green color pixels.

In order to support this claim, the relationship between the green and blue color planes in each domain is measured. However, measuring the correlation between coefficients in each domain becomes problematic. Because the blue coefficients are directly replaced with the green coefficients, a better metric is the distance rather than correlation between two color planes. A simpler Normalized Root Mean Squared Error Metric (NRMSE) is used:

$$NRMSE = \frac{\sqrt{\frac{\sum_{i=1}^{n}(X_i - Y_i)^2}{n}}}{\max(X,Y) - \min(X,Y)}. \tag{4.13}$$

Here, X and Y are the vectorized versions of the green and blue color planes in each domain.

Shown in Fig. 4.11, 64 different natural images were taken from two online

databases [44, 45]. This set of images is then compared in three different domains, the color domain, the wavelet domain, and the contourlet domain. For the contourlet and wavelet domains, information in the different sub-bands is further compared. Information about the relative distance between color planes within a domain is provided by the NRMSE. The normalization insures that this is a fair comparison and is independent of the range of a particular domain. As with the previous experiments, the images are first transformed to the wavelet domain using the db5 filter set and the contourlet domain using the db5 and PKVA8 filter sets. Five levels of decomposition are used in both domains.

Figure 4.11: The set of random images used for the NRMSE test is shown.

In table 4.1, the results of the NRMSE test are shown. For each of the rows, the lowest NRMSE is in the Green Blue NRMSE column. A strong relationship between the green and blue color planes is indicated by this trend. The middle and high wavelet coefficients have a much lower NRMSE than the color domain coefficients. This observation supports the claim that more information about high frequency components can be found in the contourlet domain than in the color domain. The FLCS is designed to maintain the sharpness of the green color plane. Post processing is used to improve the red and blue color planes.

Table 4.1: Results from NRMSE Test at different sub-bands.

Domain	Green Blue NRMSE	Green Red NRMSE	Red Blue NRMSE
Color	0.1306	0.1504	0.2252
Wavelet Low	0.1480	0.1530	0.2338
Contourlet Low	0.1419	0.1466	0.2271
Wavelet Middle	0.0267	0.0304	0.0394
Contourlet Middle	0.0215	0.0251	0.0328
Wavelet High	0.0117	0.0125	0.0159
Contourlet High	0.0117	0.0127	0.0153

4.3.4 Results from the FLCS

In Fig. 4.12, real images taken in a lab setting with a prototype of the FLCS are shown. The basic set up is a well lit room with a camera lens approximately 30 cm away from the object. The FLCS is a two lens system. The curvature of each lens is adjusted by altering the amount of liquid in the lens. By altering the curvature of the lens, the focus and magnification of the image is adjusted. More information about the testing set up can be found in [1].

In Fig. 4.13, real medical images taken with a prototype of the FLCS are shown. In this case, the image was taken in a surgical setting where the object was illuminated with a separate light source. The FLCS was approximately 6 cm away from the object. The typical effects of the algorithm on medical images are shown.

The results of the Lucy-Richardson and Wiener deconvolution are sharper than the original blurred image but these results also contain noise artifacts. An estimate of the PSF was derived from test images taken with the device. For the Lucy-Richardson algorithm, the damping parameter was set to 0.2 and 20 iterations were run. For the Wiener deconvolution, the noise-to-signal ratio was set to 0.06. Several values were tested for these parameters and the most consistent results were produced by these values. Ringing artifacts that occur in the blue images for the Wiener and Lucy-Richardson algorithms are created by this estimation error.

For the blue image set, the difference between the original image, previous

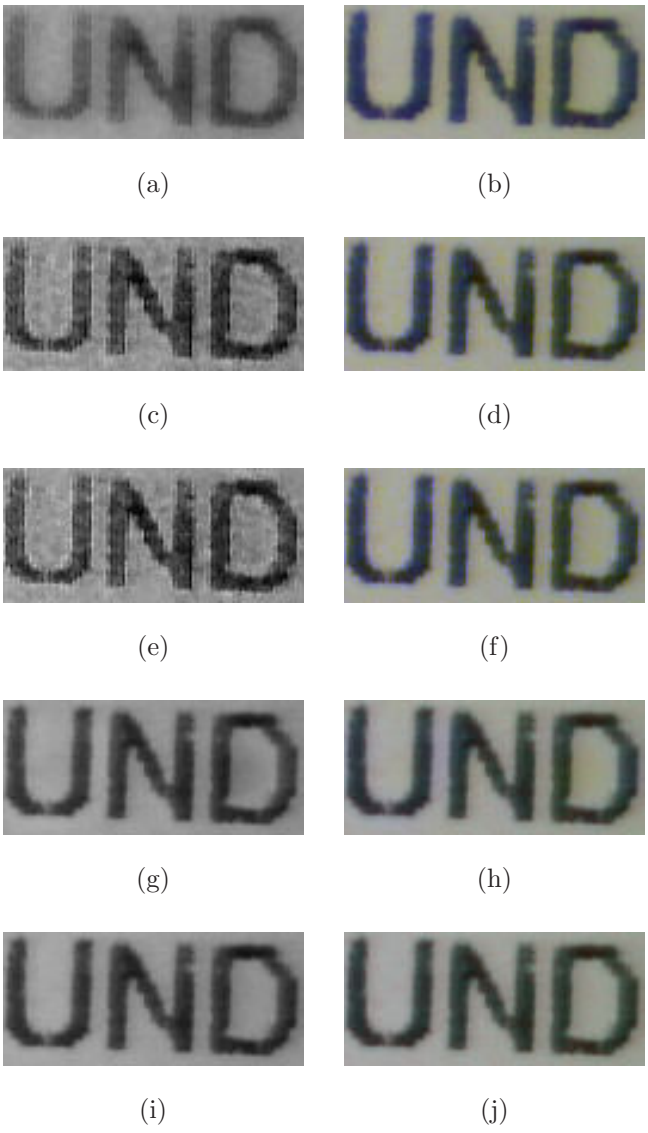

Figure 4.12: The difference between the algorithms on real data is shown. The color images must be viewed in color. (a) Original blue image; (b) original color image; (c) Wiener blue image; (d) Wiener color image; (e) Lucy-Richardson blue image; (f) Lucy-Richardson color image; (g) wavelet blue image; (h) wavelet color image; (i) contourlet blue image; (j) contourlet color image.

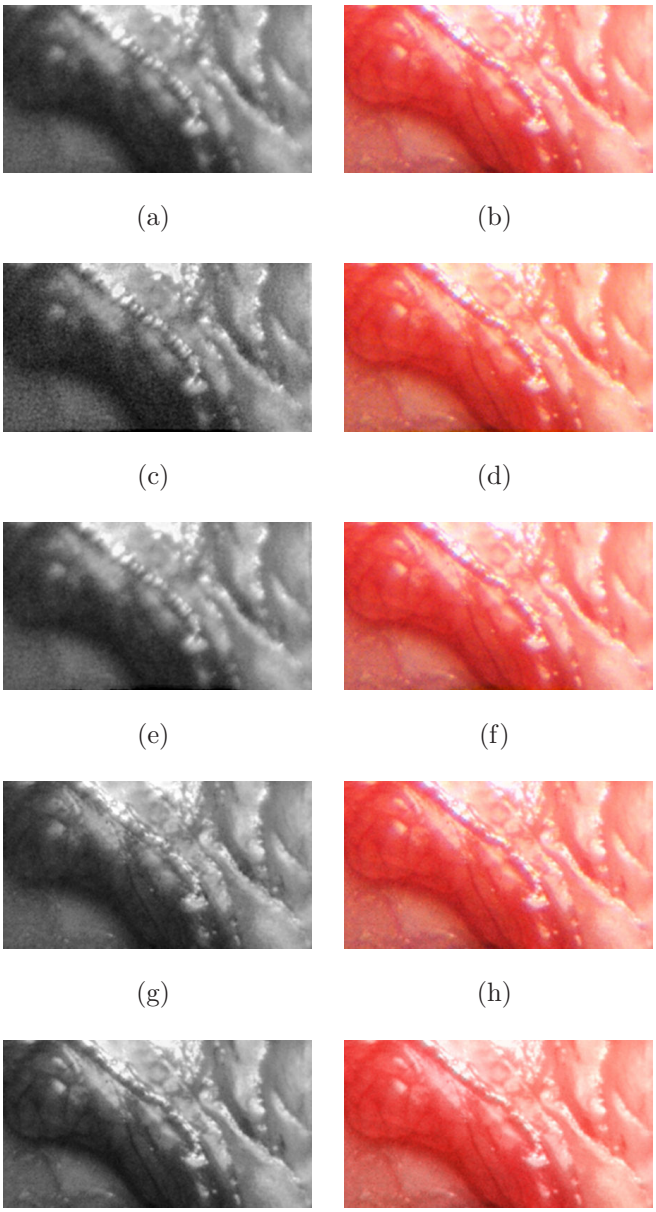

Figure 4.13: These image were taken using the FLCS in a surgical setting. The color images must be viewed in color. (a) Original blue image; (b) original color image; (c) Wiener blue image; (d) Wiener color image; (e) Lucy-Richardson blue image; (f) Lucy-Richardson color image; (g) wavelet blue image; (h) wavelet color image; (i) contourlet blue image; (j) contourlet color image.

results, and the proposed result are presented. A sharp image with consistent edges is produced by the proposed algorithm. In the color images, the color bleeding artifacts are shown. The yellowish artifacts which blur the original color image do not occur in the contourlet color image. For the proposed algorithm, estimates of the PSF are not needed and the ringing artifacts are avoided. However, the green color plane is required to be sharper than the other color planes.

The text of Chapter 4 is adapted from *Contourlet Domain Multiband Deblurring Based on Color Correlation for Fluid Lens Cameras*, Jack Tzeng, Chun-Chen Liu, and Truong Nguyen, to be published in 2010 in *IEEE Transactions on Image Processing*. The dissertation author was the primary author of these publications, the first co-author listed supplied ideas, and the second co-author listed directed and supervised the research which forms the basis for this chapter.

Chapter 5

Support Vector Regression

In Chapter 3, the Wavelet Sub-band Meshing algorithm is used to share edge information between the green and blue color planes. In Chapter 4, the Contourlet Sub-band Meshing algorithm is used to reduce color bleeding artifacts by adjusting to the natural contours of the image. These methods are general methods that do not require previous knowledge about the types of images taken with the FLCS. In this chapter, SVR is used to build prediction models. The domain is restricted to abdominal images. The edge and shading information from the FLCS image input is used to predict the pixel values. A sharp image is constructed from this prediction.

5.1 Review of Support Vector Regression

SVR is a class of supervised learning methods used to solve various regression problems [21, 22]. For a basic 2-D regression problem, the curve which best fits a series of training points is found. With this curve, future predictions can be made given one of the dimensions. With more training points, typically a more accurate curve can be produced.

During SVR, a curve is found to fit the data. As shown in Fig. 5.1, a margin is a specific radius ϵ surrounding the curve [46]. This margin is a buffer. No error is produced by all points inside this area. An error according to the loss function is produced by all points outside of this margin. A smaller ϵ is more

desirable. With a smaller ϵ, more points are outside of the margin and contribute error. This margin can be represented by support vectors. The goal of SVR is to fit a curve while minimizing the number of support vectors and minimizing the error produced by the points outside of the ϵ margin.

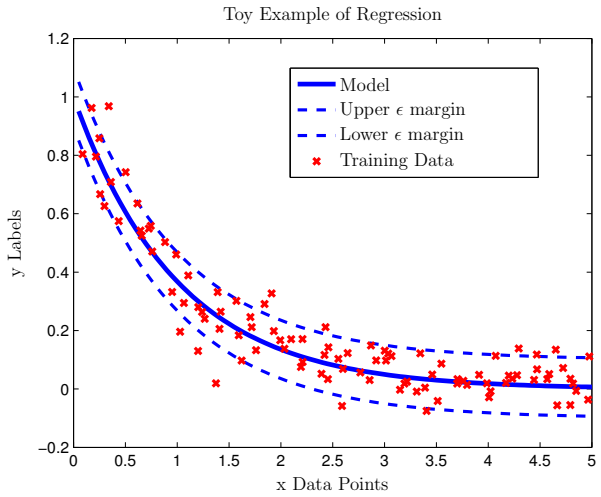

Figure 5.1: The upper and lower ϵ margin around the model are shown. Most of the training points are inside the margin.

In multiple dimensions, a hyper-plane is produced rather than a curve. With a large amount of training data, the problem $y = f(\mathbf{x})$ is solved using a multi-dimensional regression. $\mathbf{x}$ can be a multi-dimensional vector, and f is some unknown function [46]. Labels $(y_1, y_2, ...y_n)$ and the associated data $(\mathbf{x_1}, \mathbf{x_2}, ...\mathbf{x_n})$ are provided by the training set. With this training data, an estimate of the function f is produced by the SVR algorithm. During the testing phase, test data $(\mathbf{x_{t1}}, \mathbf{x_{t2}}, ...\mathbf{x_{tm}})$ is given. The labels for $(\widehat{y_{t1}}, \widehat{y_{t2}}, ...\widehat{y_{tm}})$ are predicted by the model. The amount of data supplied, the significance of the features $\mathbf{x}$, and the accuracy of the model compared to the unknown $f(\mathbf{x})$ are all factors which affect the quality of the prediction.

ν-SVR [47] is used by this algorithm. One goal of ν-SVR is to avoid high complexity models. Overfitting occurs when the training data noise is tuned while learning the model. In the overfitting case, a high complexity model is created with a large number of support vectors. During the testing phase, error is increased because the model does not generalize well. To avoid this problem, the complexity

of a model is considered during training for ν-SVR.

A brief overview of the ν-SVR algorithm taken from [48] is presented below. A more complete overview of Support Vector Machines can be found in [46]. ν is a parameter used to control the number of support vectors. The training error is balanced with the model complexity. The overall testing error is reduced. The primal form of the original problem is the following:

$$\begin{aligned} \min_{\mathbf{w},b,\xi,\xi^*,\epsilon} \quad & 0.5\mathbf{w}^T\mathbf{w} + C(\nu\epsilon + \frac{1}{l}\sum_{i=1}^{l}(\xi_i + \xi_i^*)) \\ \text{subject to} \quad & (\mathbf{w}^T\phi(\mathbf{x}_i) + b) - z_i \leq \epsilon + \xi_i \\ & z_i - (\mathbf{w}^T\phi(\mathbf{x}_i) + b) \leq \epsilon + \xi_i^* \\ & \xi_i, \xi_i^* \geq 0, i = 1, 2, ...l, \epsilon \geq 0 \end{aligned} \tag{5.1}$$

Here, $\mathbf{x}_i$ is the training vector, $\mathbf{w}$ is a weight vector which measures the complexity, ξ is a slack variable which measures the error, b is the bias, and $\phi(.)$ is the mapping to a feature space.

The dual problem is solved as:

$$\begin{aligned} \min_{\alpha,\alpha^*} \quad & 0.5(\alpha - \alpha^*)^T Q(\alpha - \alpha^*) + z^T(\alpha - \alpha^*) \\ \text{subject to} \quad & \mathbf{e}^T(\alpha - \alpha^*) = 0, \mathbf{e}^T(\alpha + \alpha^*) = Cl\nu \\ & 0 \leq \alpha_i, \alpha_i^* \leq C, i = 1, ...l. \end{aligned} \tag{5.2}$$

Here, $Q_{ij} = K(\mathbf{x_i}\mathbf{x_j})$ is defined to be $\phi(x_i)^T\phi(x_j)$. The kernel function used in this chapter is the radial basis function. A decision function for the SVR is produced.

$$\sum_{i=1}^{l}(-\alpha_i + \alpha_i^*)K(\mathbf{x_i}, \mathbf{x}) + b \tag{5.3}$$

The number of support vectors is minimized using this algorithm. Overfitting the training data is avoided and the testing error is reduced.

5.2 The Algorithm

A Two-Stage SVR system is proposed in this chapter. In order to train an SVR, training data with the training features $\mathbf{x}$ and the output value y are provided. During testing, the data points $\mathbf{x}'$ are given to the model and the labels y' are predicted. These ideas can be expanded to multiple dimensions for $\mathbf{x}$ and a hyperplane that predicts the value of y is produced.

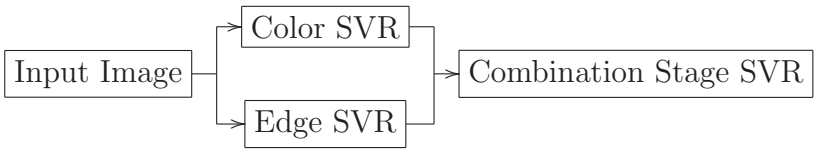

Figure 5.2: This flowchart shows the Two-Stage SVR

A set of sharp medical images taken from a conventional laparoscope is used as the training data for this model. During training, the data sets were drawn uniformly at random from a set of 50,000 data points. For all the SVR models, the data was produced from the same underlying set of images. As shown in Fig. 5.2, the algorithm presented is a two-stage system with three separate SVRs: a Color SVR in the color domain, an Edge SVR in the contourlet domain, and an SVR to combine the two other SVRs.

A different purpose is served by each regression. The blur is reduced by the Edge SVR. Consistent color is maintained by the Color SVR. Information is combined by the Combination Stage SVR. As shown in Fig. 5.3, each model is composed using a few basic steps: transform to a specific domain, vectorize the data, run the prediction, inverse the vectorization, and inverse the transformation back to the color domain. A C++ library called LibSVM [48] is used for the underlying library of functions for the SVR.

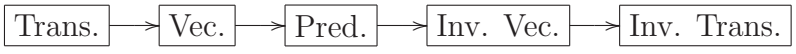

Figure 5.3: This flowchart shows the SVR modeling setup

5.2.1 Color Support Vector Regression

The SVR is performed in the color domain. A transformation is not required for this model. The green and red of components of the image are used to predict the blue component.

1. Each image is separated into the R, G, and B color planes.
2. An SVR is constructed based on the color data.
3. Each color plane is vectorized into (r, g, b) and $\mathbf{x} = (r, g)$ and $y = (b)$ are used to construct a SVR model.
4. The predicted values for y_{p1} are used to construct a predicted blue image b_1.

The color gamut of visible light can be thought of as a 3-D space in RGB. For a 24 bit color image, 256^3 possible values are contained in this color gamut. A 2-D surface model in this color space is created by the SVR. This 2-D surface is limited to 256^2 possible color values. Colors represented in the human body are chosen by the SVR. By limiting the training data to medical images, a 2-D surface is created which encompasses all colors expected to appear in the abdomen. False colors not observed in the human body are produced by noise and color blur. These artifacts are reduced by this SVR. The number of features in this SVR is two, one feature from the green color plane and one feature from the red color plane.

5.2.2 Edge Support Vector Regression

An Edge SVR is constructed in the first stage of the system. The image is first transformed into the contourlet domain to separate the edge components from the shading components. Once in the contourlet domain, the green and the red contourlet coefficients are used to predict the blue contourlet coefficients.

1. The R, G, and B color planes are transformed into the contourlet domain.
2. The contourlet domain can be partitioned into several levels, for each level a separate model is trained using the $\mathbf{x} = (r_c, g_c)$ and $y = (b_c)$.

3. The predicted y_{p2} values are used to invert the contourlet transformation and to construct a predicted blue image b_2.

The construction of this model is much more complex than the other ones. The levels of the contourlet decomposition was chosen to be the [2,2,2,2] set. Four high frequency levels of decomposition are produced. For each level, the spectrum is broken up into four neighboring directions. A low band frequency level with only one direction is added as an additional direction. One coefficient is contributed by each direction. 17 different contourlet coefficients are created. In Fig. 5.4, the coefficients are grouped by frequency level and then by neighboring direction.

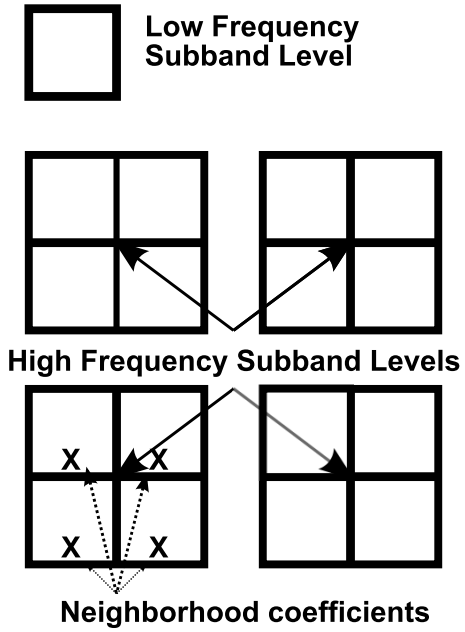

Figure 5.4: The contourlet decomposition is shown in this diagram. Four high frequency sub-bands each with four neighborhood coefficients as well as one low frequency sub-band are shown.

Accurate data is required for the SVR prediction method. An accurate prediction cannot be obtained, due to excessive noise in the highest frequency sub-band. The green contourlet coefficients are directly used for all four directions in the highest frequency sub-band. The remaining 13 directions are predicted using SVR.

Described above is the basic set up of the prediction. 13 different models are produced by this setup, one for each direction. The blue contourlet coefficients are used for the labels. For the features $\mathbf{x}$, the four red and four blue neighboring contourlet coefficients are used. The lowest frequency green coefficients are used to predict the lowest frequency blue coefficients with no neighboring coefficients.

After the prediction of the blue contourlet coefficients, the result is transformed back to the color domain. The goal of this model is to sharpen the blue image. By learning from sharp edges, the blur is reduced. The contourlet coefficient space is limited to sharp edge coefficients.

5.2.3 Combination Stage Support Vector Regression

For each of the previous regressions, the space of possible values is limited to those desired for the system. The space of possible color values is limited by the Color SVR to colors in the human body. The space of possible contourlet coefficients is limited by the Edge SVR to sharp edges. These two models are combined by this final SVR.

1. Using the two predicted blue images found in Section 5.2.1 and Section 5.2.2, a combination stage is introduced.

2. b_1 and b_2 images are vectorized and a third SVR model is trained with $\mathbf{x} = (b_1, b_2)$ and $y = (b)$.

3. With the predicted values for y_{p3}, a predicted blue image b_3 is constructed.

The results from each of the previous models are used to predict a sharp blue image. The color model is used to predict color data consistent with the internal human body. The contourlet model is used to produce sharp edges. Color bleeding produced by previous algorithms is avoided by this combination stage. The sharpness from the contourlet model is maintained. To generate the training set for this SVR, the image results of the previous two SVR's were used as training data. The original sharp blue images were used as labels. The number of features in this SVR is two, one feature from the Color SVR result and one feature from the Edge SVR result.

5.2.4 Testing Algorithm

Three different models are constructed by the proposed Two-Stage regression. During the testing phase, a simpler algorithm is used.

1. A color image from the device is provided with a sharp green image and a blurred blue image.

2. The R, G, and B images are vectorized. The data $\mathbf{x} = (r, g)$ is used with the Color SVR Model trained in Section 5.2.1 to predict the labels b_1.

3. The R, G, and B images are transformed into the contourlet domain. The data $\mathbf{x} = (r, g)$ is used with the Edge SVR Model trained in Section 5.2.2 to predict the labels y_{p2}. The inverse contourlet transform is used to construct a predicted b_2.

4. The $\mathbf{x} = (b_1, b_2)$ is used with the Combination Stage SVR Model trained in Section 5.2.3 to predict the labels $y = b_3$.

5.3 Results

5.3.1 Simulated Image Test

The results of learning the Two-Stage implementation discussed in the previous section are shown in Fig. 5.5. Sets of 500, 5000, 10000, and 20000 random points are applied to the various SVR methods. This modeling was repeated over 20 iterations. For each iteration, a new set of random points was selected. A two-fold cross validation scheme was implemented to find the best parameters for the SVR. Overfitting of the data is prevented by this cross validation. For all of the training, a radial basis function (RBF) kernel was used. For every model produced, model parameters for ν-SVR were created by the cross validation. Through testing, $\nu = 0.5$ and the cost parameter $0.5 \leq c \leq 8$ were found to be a good range. The width of the RPF kernel is set $0.5 \leq \gamma \leq 8$. Based on the results of the cross validation, a slightly different set of parameters is used by each of the 20 iterations.

Once the system has learned these models, the system was tested with a new set of images. These images were taken using a sharp laparoscopic camera. A Gaussian blur window of 15 x 15 with a standard deviation of 15 was convolved with that image to simulate blur. The Gaussian blur window was chosen because it resembles the blurring from the lens. The 20 different Two-Stage models were then used to produce the resulting deblurred image. The average PSNR between the deblurred image and the original sharp image are presented in the graph. In addition, the errors representing one standard deviation are presented as well.

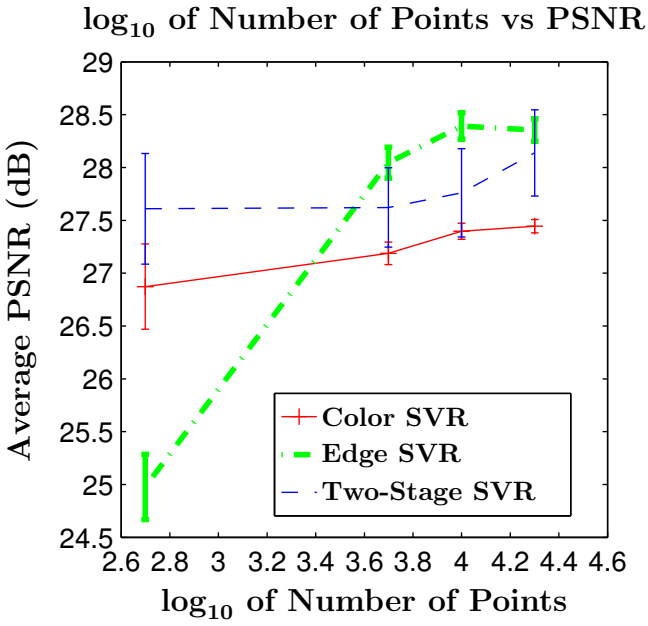

Figure 5.5: The effects of the number of training data points for the SVR using only green data are shown.

The effects of the Two-Stage implementation are shown in Fig. 5.5. The model is trained using sharp green data with the blue and red color planes blurred. As the number of training points is increased, the standard deviation is decreased. The PSNR is improved by the Two-Stage SVR method over the Color SVR method. Both the edge and the color information are required to produce the best results. As the number of training points is increased, a flattening out is seen in the Color SVR and Edge SVR curves. However, continued improvement is seen in the Two-Stage SVR curve. This effect suggests that the Two-Stage model has a higher upper bound in the gains produced by these regressions. More points are required

for the Two-Stage model to fully realize the algorithm's potential to reduce blur.

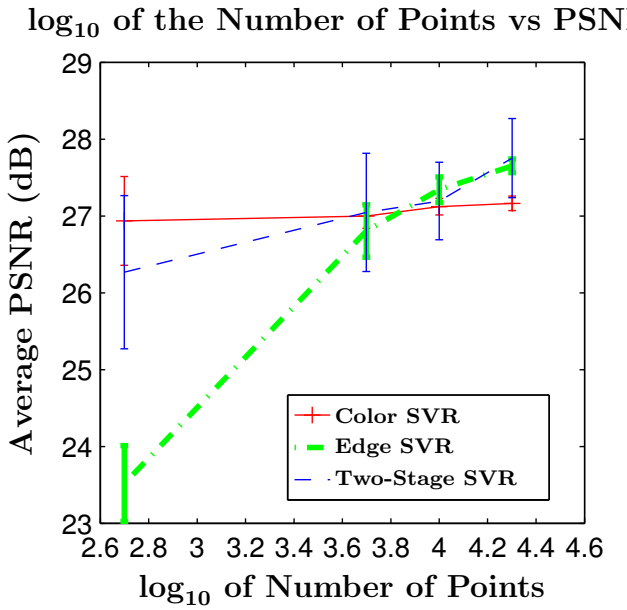

Figure 5.6: The effects of the number of training data points for the SVR using red data and green data are shown.

The results of training the system using sharp data from both the green and red images are shown in Fig. 5.6. For the previous figure, the model is trained using the sharp data from the green color planes. In the actual liquid lens, the red image is moderately blurred under certain magnifications. By training from the green and red color planes, the number of feature dimensions used is doubled. While the Color SVR and Edge SVR decrease in standard deviation as the number of points increases, the standard deviation for the Two-Stage SVR is stable. The PSNR is high for the Two-Stage SVR. As indicated by the graph, a minimum of 5000 points is required for the Two-Stage SVR to consistently produce a higher PSNR than the Color SVR. The Color SVR is able to train quickly. A small number of points is required to be effective. At 20,000 points, better results than the other two models on average are achieved by the combination stage model. As indicated by the large standard deviation, more data must be trained to yield stronger conclusions about the effectiveness of training on multiple color planes.

A sample output of the Two-Stage implementation is shown in Fig. 5.7. The results from the Color SVR, Edge SVR, and Two-Stage SVR are shown in the

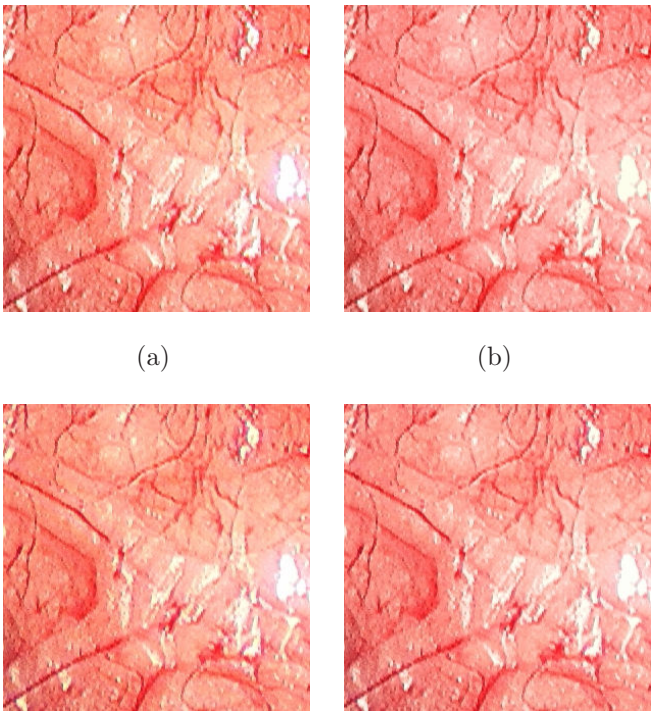

(a) (b)

(c) (d)

Figure 5.7: The edge and shading information is combined using the Two-Stage SVR. These images are best viewed in color. (a) Original color image; (b) predicted image using Color SVR (c) predicted image using Edge SVR; (d) predicted image using Two-Stage SVR.

figure. Using the original color image, blur is introduced. To test how accurately the SVR would reproduce the original color image, the Two-Stage implementation is then run. The goal of these algorithms is to produce an image as close as possible to the original image. The correct colors for the image are extracted by the Color SVR. The edges of the system are enhanced by the Edge SVR. These two pieces of data are combined in the Combination Stage SVR, making the model more robust to noise and to blur.

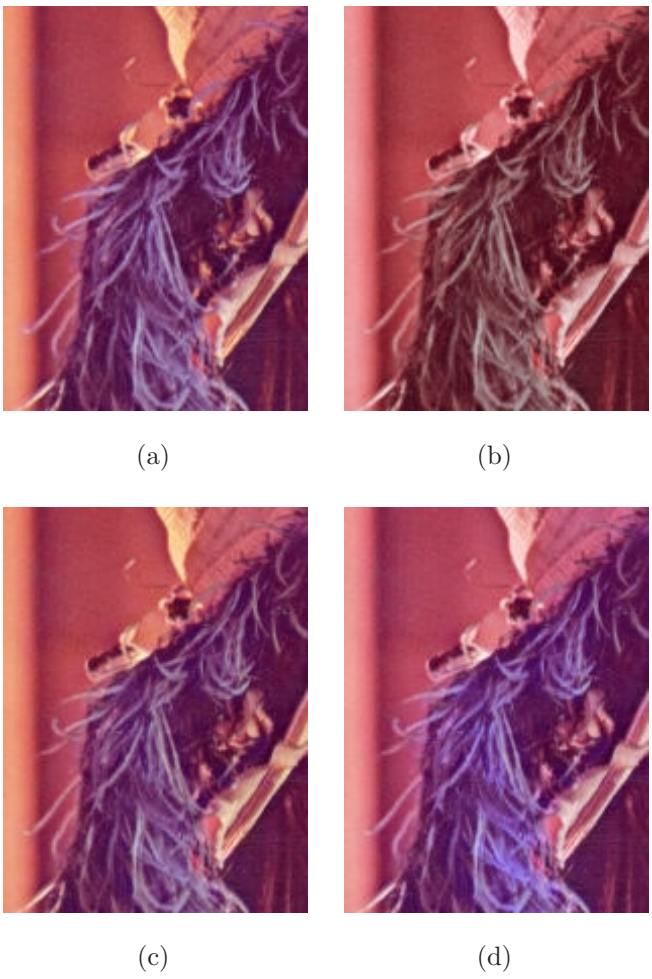

(a) (b)

(c) (d)

Figure 5.8: The results of applying the model on non-medical images are shown. This image is best viewed in color. (a) Original color image; (b) predicted image using Color SVR; (c) predicted image using Edge SVR; (d) predicted image using Two-Stage SVR.

The results of implementing the algorithm on non-medical data are shown

in Fig. 5.8. The original training set of medical image data is performed by the proposed algorithm. A problem for the Color SVR is presented by this training set. Incorrect predictions are suffered when applying this model to non-medical images. Poor results are produced by the color surface created by the SVR. The PSNR is severely degraded by the change in colors. The Edge SVR results are not affected by the change in domain. Sharp and blurry images are differentiated by the Edge SVR. The sharp non-medical test images are produced by the Edge SVR. As shown in this example, the Edge SVR is more robust to changes in the training data.

The results as the blur increases for the blue image are shown in Fig. 5.9. The degree of blur added to the input is represented by the size of the Gaussian blur kernel. Previous methods begin to degrade as more blur is added to the system. The proposed method is able to remain stable. The green and red data are used to train this method. The reconstruction results are marginally affected by the increase in blur of the blue data. At different spatial locations and different magnifications, the PSF of the FLCS is changing. The proposed method is robust to these variations in the PSF. Once the model has been trained, multiple degrees of blur can be corrected.

5.3.2 Computation Costs

All simulations were run on an Intel Core 2 Duo CPU with a 3.00 GHz processor at 3.0 GB of RAM. All algorithms are run using Matlab. Depending on the number of training points, training all of the SVR models can take a few minutes with 500 points to several days with 20,000 points. The computation times are compared in Table 5.1 of various algorithms during the testing phase.

For the proposed algorithm, linear growth with respect to the size of the image and the number of training points is shown in Table 5.1. The implementations of the Richardson-Lucy, Wiener, and Total Variation method using $TV/L1$ [27] is faster than the proposed method. However, these algorithms all rely on accurate PSF estimation. For the FLCS, an accurate PSF cannot be produced.

A comparison of PSNR results is shown in Table 5.2. At the largest image

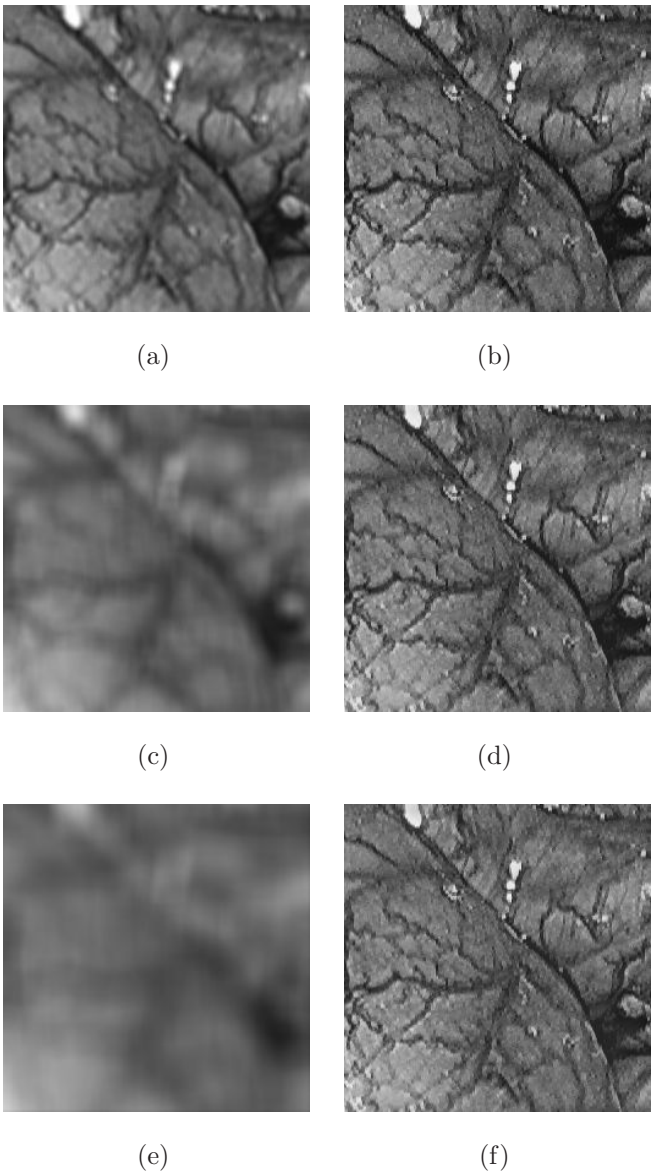

(a) (b)

(c) (d)

(e) (f)

Figure 5.9: As the blur level of the input image increases, a similar level of consistency in terms of sharp edges is maintained by this SVR. (a) Blur image at 5 pixel wide blur; (b) Two-Stage SVR image for 5 pixel wide blur; (c) blur image at 17 pixel wide blur; (d) Two-Stage SVR image at 17 pixel wide blur; (e) blur image at 29 pixel wide blur; (f) Two-Stage SVR image at 29 pixel wide blur.

Table 5.1: A comparison is shown of the computation time in seconds required to deblur a test image. The following methods are analyzed: Richardson-Lucy, Weiner, Contourlet Sub-band Meshing, Total Variation, and Proposed with 500-20000 training points.

Image Size	RL	Wiener	Cont-ourlet	TV	Prop. 500	Prop. 5000	Prop. 10000	Prop. 20000
128x128	0.15	0.022	0.142	1.70	1.91	12.8	25.2	49.2
256x256	0.46	0.072	0.379	5.68	6.64	49.8	97.5	193.0
512x512	3.57	0.403	1.689	27.98	27.5	200.1	390.9	778.9

Table 5.2: A comparison is shown of the PSNR in dB. The following methods are analyzed: Richardson-Lucy, Weiner, Contourlet Sub-band Meshing, Total Variation, and Proposed with 500-20000 training points.

Image Size	RL	Wiener	Cont-ourlet	TV	Prop. 500	Prop. 5000	Prop. 10000	Prop. 20000
128x128	19.72	25.52	23.41	24.37	25.64	25.76	25.82	25.99
256x256	20.24	24.60	24.87	24.12	27.97	27.86	27.96	27.79
512x512	21.26	24.50	26.73	23.68	27.61	27.62	27.76	28.14

size, the contourlet deblurring method is able to achieve results 2 dB higher than conventional methods. The proposed method is able to achieve slightly higher results than the contourlet-based method. For the largest image size, better results are achieved by the proposed method as the number of training points increases.

For this test, the Richardson-Lucy algorithm was given the exact PSF and run for 10 iterations. The Contourlet Sub-band Meshing algorithm was run on four levels of decomposition. The Total Variation method was given the exact PSF. Only the test times are listed and the training is assumed to have been completed.

5.3.3 Real Image Test

Images taken during a pig experiment from a prototype of the FLCS are used in this section. Surgical incisions were made on a pig and the FLCS was inserted into the abdomen. As shown in Fig. 5.10, incorrect coloring with a yellowish tint and blurring of the original images are caused by the lens. The best

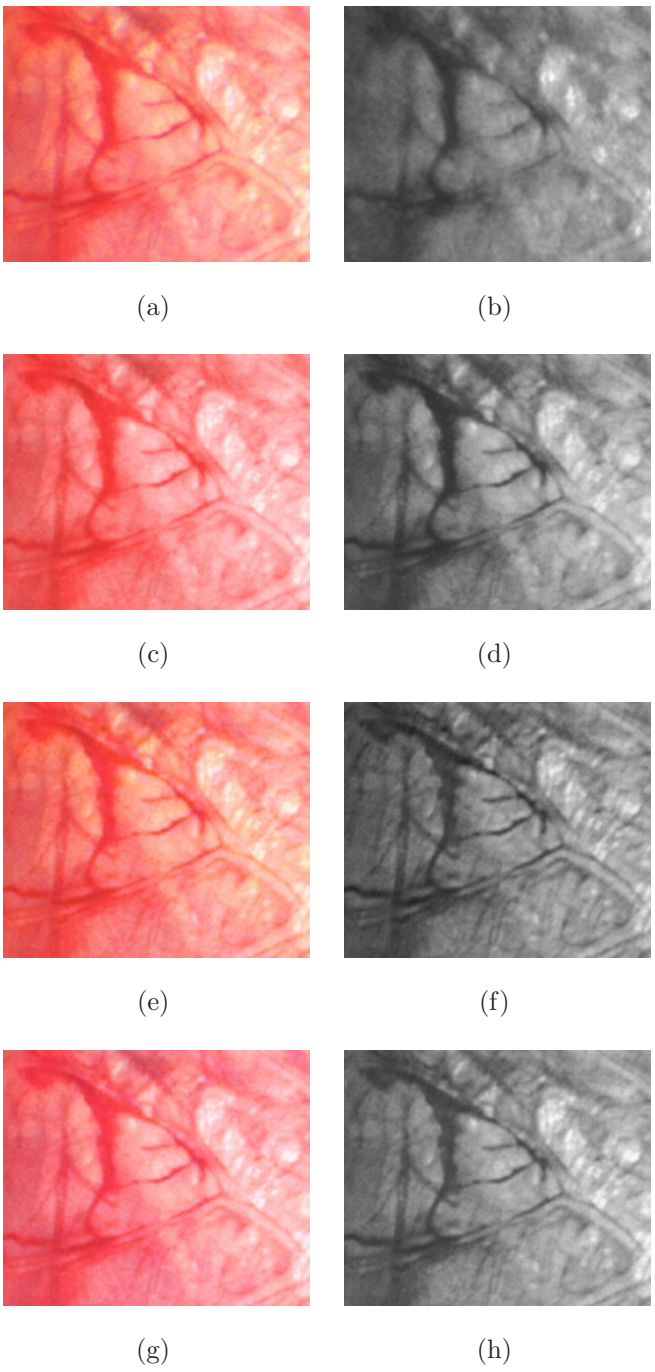

Figure 5.10: Once the blue image has been sharpened, the yellowish blur is removed from the color image. (a) Original blurred color image; (b) original blurred blue image; (c) Color SVR color image; (d) Color SVR blue image; (e) Edge SVR color image; (f) Edge SVR blue image; (g) Two-Stage SVR color image; (h) Two-Stage SVR blue image

color results are produced by the Two-Stage SVR. The yellow tint is removed by this method. For the blue image results, after each SVR, the edges become more refined. The blur of the blue color planes are reduced by the proposed algorithm.

Images from several algorithms are shown in Fig. 5.11. The goal of each algorithm is to remove the blur and to sharpen the edges. Regularization noise is seen in the results from the Richardson-Lucy deconvolution and Wiener deconvolution. A lack of sharpness is seen in the Total Variation method. Only a rough estimate of the PSF is provided to this method. The edges that were lost during blurring are not recovered by this algorithm.

Stronger edges are seen in the Contourlet Sub-band Meshing [16] results. The shading of the image is not maintained. The edge results of the image are improved by the Two-Stage proposed algorithm. The correct levels of shading are also maintained by the proposed method. [1]

The text of Chapter 5 is adapted from *Multiband Deblurring using Support Vector Regression for Fluid Lens Cameras*, Jack Tzeng and Truong Nguyen, submitted February 2010, in preparation for *IEEE Transactions on Image Processing*. The dissertation author was the primary author of these publications, and the co-author listed directed and supervised the research which forms the basis for this chapter.

[1] More simulation results are available at: http://videoprocessing.ucsd.edu/∼jack865/TIP3SVR/index.html

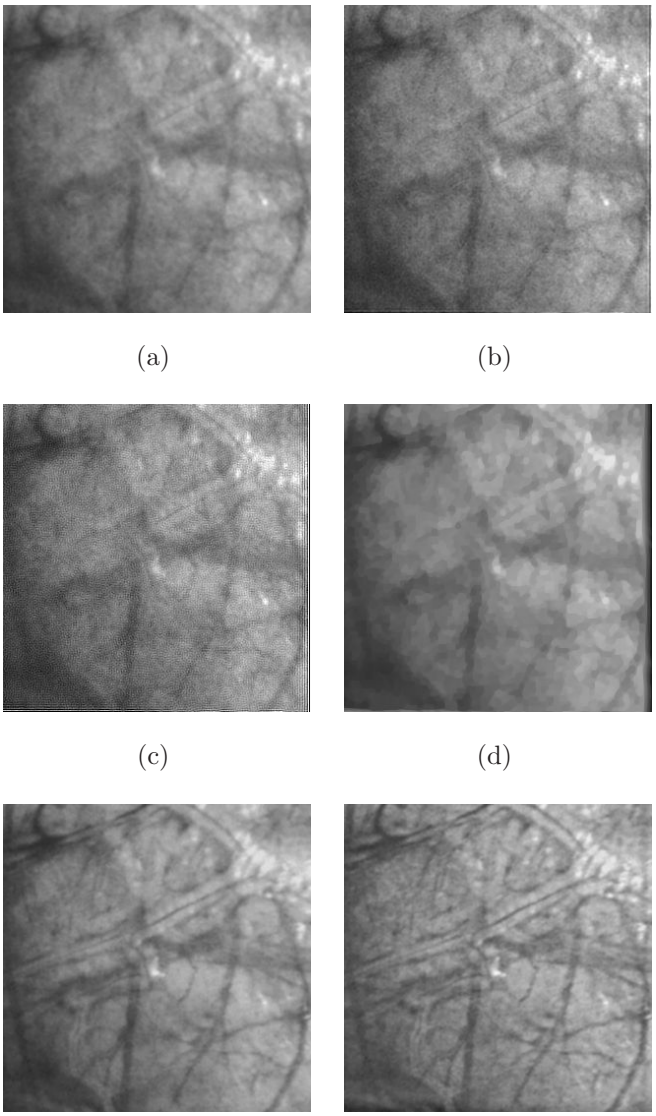

(a) (b)

(c) (d)

(e) (f)

Figure 5.11: The differences between various algorithms are shown in this real image test. (a) Original Blurred Blue Image; (b) Richardson-Lucy deconvolution; (c) Wiener deconvolution; (d) Total Variation; (e) Contourlet Sub-band Meshing; (f) Two-Stage proposed algorithm.

Chapter 6

Adaboost Classification

In this chapter, three previous methods are considered: a contourlet-based method, a Color SVR in the color domain, and an Edge SVR in the contourlet domain. Adaboost is used to combine the three methods to produce a sharp image. The goal of this classification is to determine which algorithm will succeed in different areas of the image. Once the predicted algorithm is applied to each pixel location, the images that are produced have less error than each component method.

6.1 Background

6.1.1 Adaboost

Adaboost is a method for turning a series of weak classifiers into one strong classifier [49]. In the first iteration, every training point is given an equal weight and a weak classifier is applied by the algorithm. Points which have been correctly identified are given a small weight, while points which are incorrectly identified are given a large weight. For the next iteration step, a new classifier is added and points with higher weight are more heavily focused on. The weights are readjusted to focus on any points which have been misclassified and the iteration step is repeated. This iterative approach is used until convergence of the classification training error [50].

An important component of Adaboost is the type of features used. Features which discriminate between the classes are the most useful. The spatial derivatives, local pixel values, color derivatives, and contourlet ratio are all used as features of this system.

In order to produce labeled training data, a blue image is blurred using a Gaussian kernel. Each of the three methods is applied. Every pixel is labeled with the method that produced the result closest to the sharp blue image. The features for each of the pixels are also calculated. These labels and features are used by Adaboost to build a strong classifier. Once a strong classifier is built, every pixel location is classified into one of the three classes.

6.1.2 Mean Noise Filter

After the strong classifier created by Adaboost is run, an image map is created. The pixel locations where the algorithm believes each method will succeed is represented by the image map. This choice is a hard decision boundary and a pixel is chosen to be in one of the three classes. In certain instances, different classes may be chosen for neighboring pixels. If the results of each component method are significantly different, artifacts are caused by this method. The neighboring pixels are not blended well by the algorithm.

To reduce these artifacts, a soft transition between pixels is created. A 3x3 window is swept across the image map. At each pixel location, the classes given to each of the 9 pixels in a neighborhood window are collected. Three coefficients are calculated, the percentage of pixels in the 3x3 neighborhood which fall into each of the three classes is defined by these coefficients. A weighted average of the local results from the classifier is represented by these coefficients. Areas where multiple pixels are classified as a particular class will have a high coefficient for that class. At each pixel location, these coefficients are multiplied with the image result from each of the three respective methods. The final result is a weighted average at each location of the output from the three methods, $\tilde{B}_i$, as shown in (6.1). A soft transition between pixels is produced by this weighted averaging.

$$\tilde{B}(x) = c_1(x)\tilde{B}_1(x) + c_2(x)\tilde{B}_2(x) + c_3(x)\tilde{B}_3(x) \tag{6.1}$$

Here, c_i is the weighting coefficient at each pixel location for each method. $\tilde{B}_i$ is the output from each individual method. $\tilde{B}$ is the final output of the system.

6.2 The Algorithm

1. The Contourlet Sub-band Meshing algorithm is applied. The high frequency edge information is extracted from the green channel and is applied to the low frequency edge information from the blue channel. An estimate of the Blue image, $\tilde{B}_1$, is formed.

2. The Color SVR is applied. The red and green pixel values are used to predict the blue pixel values at every location. An estimate of the Blue image, $\tilde{B}_2$, is formed.

3. The Edge SVR is applied. The contourlet coefficients at every location are predicted using the red and green contourlet values. The image is reconstructed back to the color domain. An estimate of the Blue image, $\tilde{B}_3$, is formed.

4. The features that will be used by Adaboost are calculated. The spatial derivatives, local pixel values, color derivatives, and contourlet ratio are all used as features of this system.

5. Using the features, the strong classifier is applied. Each point is classified into one of the three classes.

6. In order to reduce noise, the mean noise filter is applied to the mapping. Three coefficients at each pixel are produced which represent the weight of each method.

7. Using (6.1), the entire image is processed. The final estimate, $\tilde{B}$, is produced by using $\tilde{B}_1$, $\tilde{B}_2$, and $\tilde{B}_3$ as well as the three coefficients formed by the previous step.

6.3 Results

In this section, experimental results are presented. Simulation results are shown by taking a sharp image and blurring it with a blur kernel and adding noise to the system. Non-medical and medical images are analyzed. Graphical results are presented which compare the proposed algorithm against the Contourlet Sub-band Meshing algorithm as well as two metrics using both AGWN and Poisson noise. Experimental results are also presented showing images taken from the FLCS. For the contourlet method, the Daubechies (db5) [19] filter set is used for the pyramidal structure and the PKVA8 filter set [42] is used as the directional filter. Between four to eight levels of decomposition were used to maximize the performance of the contourlet-based algorithm.

6.3.1 Simulated Images

In Fig. 6.1, a sample medical image is shown running the contourlet method and the proposed method. For this test, the original blue image in Fig. 6.1(a) is blurred with a size 21x21 Gaussian kernel with a variance of 50. AWGN noise with a standard deviation of 0.25 has also been added to form Fig. 6.1(b). In Fig. 6.1(e), the absolute difference between the contourlet method results and the proposed method results is shown. This image has been scaled and inverted to make the differences appear more clearly.

Looking at the difference image in Fig. 6.1(e), the largest differences are along the edges of the rim in the right side of the image and the dark lines that appear on the left of the image. While the two result images appear to have the same level of sharpness, the difference is in the level of shading. A closer level of shading to the original image is produced by the results of the proposed method.

The proposed method is a mixture method that uses the Color SVR and

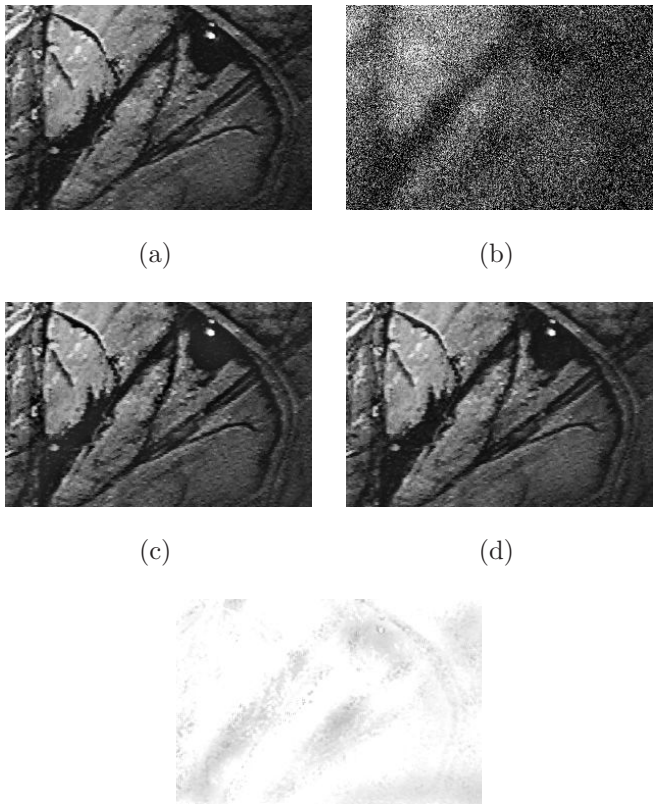

(a) (b)

(c) (d)

(e)

Figure 6.1: On medical images, the proposed algorithm reduces false coloring artifacts. (a) Original blue image; (b) blurred and noisy blue image; (c) contourlet method; (d) proposed method; (e) difference image between (c) and (d).

Edge SVR in areas where the original contourlet algorithm has failed. The lowest sub-band of the blue image is affected by the AWGN. The blue shading values of the contourlet algorithm are dependent on the lowest sub-band. In the Color SVR case, the blue shading values are dependent on the red and green pixel values. The Color SVR is not affected by noise in the blue image. During the classification step, the Color SVR is chosen for certain pixels to compensate for the shading problems in the contourlet method.

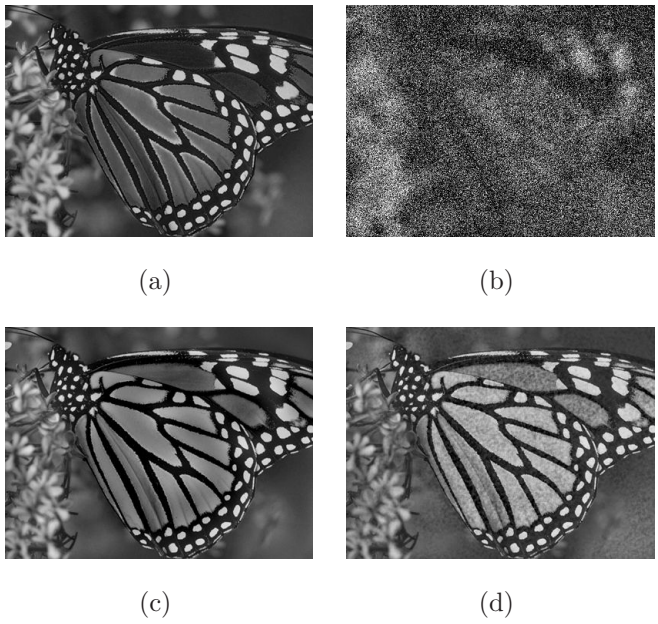

(a) (b)

(c) (d)

Figure 6.2: On non-medical images, the proposed algorithm contains noise artifacts. (a) Original blue image; (b) blurred and noisy blue image; (c) contourlet method; (d) proposed method.

In Fig. 6.2, a sample image is shown of the results of each method on non-medical images. For this test, the original blue image in Fig. 6.2(a) is blurred with a size 21x21 Gaussian kernel with a variance of 50. AWGN noise with a standard deviation of 0.25 is added to the image. The edges of the butterfly are reconstructed by the contourlet method because those edges are from the unblurred green image. The lowest sub-band is altered by the noise in the blue image which affects the shading values along the wing.

The output of the proposed algorithm is significantly affected by the change in domain. Because the butterfly is not in the same domain as the training set of

medical images, several steps are affected. During the training stage of the Color SVR and Edge SVR, the initial data set is composed of abdominal images. A 2-D surface of colors found in the abdomen is formed by the Color SVR. The colors produced by the butterfly are not found in the human body and the prediction is poor. The classification algorithm is dependent on features found in the abdomen. Poor classification results are produced by the change in domain. Noise artifacts are produced by the algorithm.

6.3.2 Graphical Results

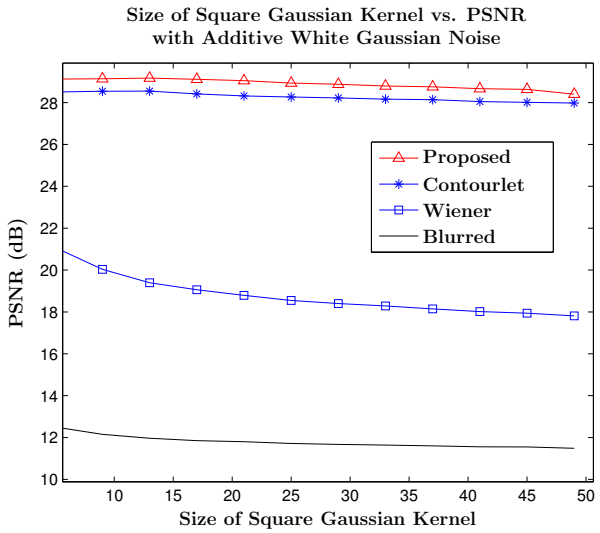

Figure 6.3: The proposed algorithm achieves the highest PSNR.

In Fig. 6.3, the effects of increasing the size of the square Gaussian blur kernel under AWGN are shown. Here, the standard deviation of the AWGN is fixed at 0.2 and the mean is 0. The image is blurred by a square Gaussian blur kernel. The size of the kernel is increased from 5x5 to 49x49. The blue channel is the only channel which has been altered, the red and green channels are assumed to be clean and unblurred. For a small kernel size, the PSNR of the outputs from the proposed method and the Contourlet Sub-band Meshing method are close. As the blur increases, the image quality of the proposed algorithm is stable, while the image quality of the Contourlet Sub-band Meshing algorithm is lower.

For comparison, the conventional Wiener deconvolution method is run. For this test, the Wiener deconvolution method was given the exact PSF as well as the noise and signal autocorrelation functions in order to maximize results. Lucy-Richardson deconvolution is not run because a Poisson noise statistic is assumed for that method.

The contourlet method is more affected by the increase in the size of the blur kernel. The lowest sub-band of the blue image and the other sub-bands from the green image are used by the contourlet method. As a result, the shading component of the reconstruction is affected by blur and noise while the edge component is not. The Color SVR is a prediction method that uses data from the green and the red color planes. This SVR is not affected by blur in the blue channel. The blue contourlet coefficients are used by the Edge SVR and that method is affected by the blur. Using the strong classifier, the proposed method is more robust to blur. Using the Color SVR, the areas of the image where noise disrupts the contourlet method are improved by this classification method. The loss in shading quality from the contourlet image is compensated for by the strong classifier.

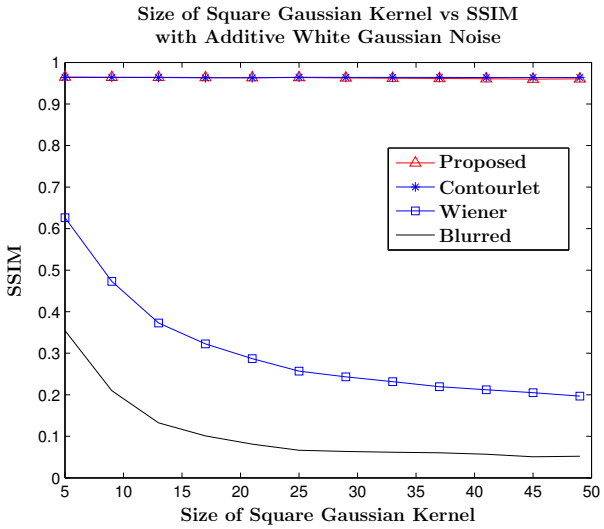

Figure 6.4: The proposed algorithm achieves an equivalent SSIM to the contourlet method.

In Fig. 6.4, the same experiment as in Fig. 6.3 is run, and the SSIM is shown. The contourlet and the proposed algorithm have very similar SSIM values. A higher SSIM than the conventional Wiener deconvolution method is achieved by

both these methods.

SSIM is an image quality metric which looks at the sharpness and the local variance of an image against the unblurred reference image [43]. The SSIM of the two methods is very close while the PSNR deviates. This difference between the results of the two metrics is an indication that the two methods produce similar levels of sharpness and different levels of shading. Because the proposed method uses the contourlet method in several areas, the sharpness of the two methods is similar. The shading values differ when the Color SVR and Edge SVR methods are chosen by the strong classifier.

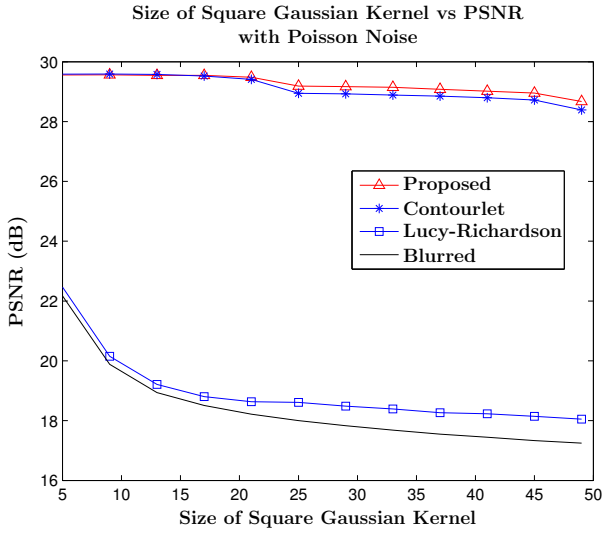

Figure 6.5: The proposed algorithm achieves the highest PSNR.

In Fig. 6.5, the image is blurred by a Gaussian blur kernel. Poisson noise is added to the blurred image. The size of the square Gaussian kernel is increased from 5x5 to 49x49. The variance of the Gaussian kernel is fixed at 50. For comparison purposes, the Lucy-Richardson algorithm is run. The regularization parameter for the Lucy-Richardson algorithm ranges from [0-0.2], whichever values maximized the PSNR. Wiener deconvolution is not run because that method assumes AWGN.

In low levels of blur, when Poisson noise is added, the two methods have comparable results. As the blur kernel size increases, the image quality of the contourlet method is reduced. A stable PSNR is maintained by the proposed method. As noted earlier, the Color SVR method is not dependent on the blur in

the blue channel. Results that are more robust to the blur in the blue channel are developed by the strong classifier.

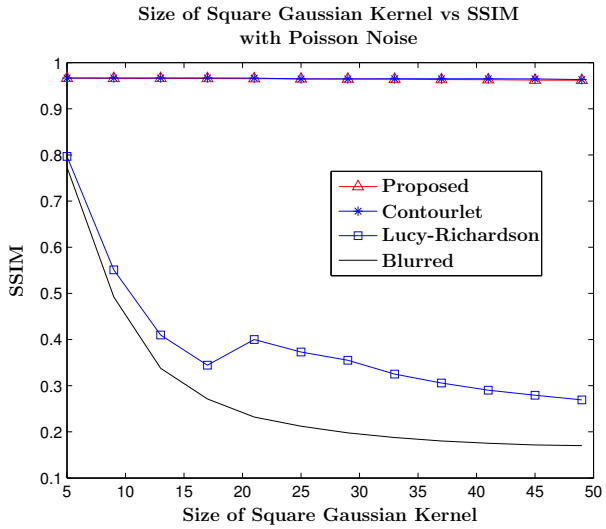

Figure 6.6: The proposed algorithm achieves an equivalent SSIM to the contourlet method.

In Fig. 6.6, the same test is performed as in the previous figure and the SSIM is measured. The SSIM of the proposed method and the contourlet method are extremely close because the edge structure of the two methods is similar. The same regularization parameter used in Fig. 6.5 are used for the Lucy-Richardson algorithm. The slight bump in the Lucy-Richardson graph at size 21x21 comes from the fact that for each size the regularization parameter was chosen to maximize the PSNR. This region is a transition region for the regularization parameter.

In Fig. 6.7 and Fig. 6.8, the effects of increasing the variance of the white noise are described. The AWGN mean is fixed at 0. The blur kernel is fixed at 15x15 with a variance of 15. The PSNR of the proposed algorithm and the Contourlet Sub-band Meshing algorithm are initially close. However, as the noise increases, the Contourlet Sub-band Meshing algorithm begins to degrade while the proposed algorithm is more robust to the increase in noise. The Wiener deconvolution method is given the exact PSF used to blur the image as well as the autocorrelation functions of the noise and the original image.

For low levels of noise, similar levels of PSNR are achieved by the proposed algorithm and the contourlet algorithm. For high levels of noise, the PSNR of the

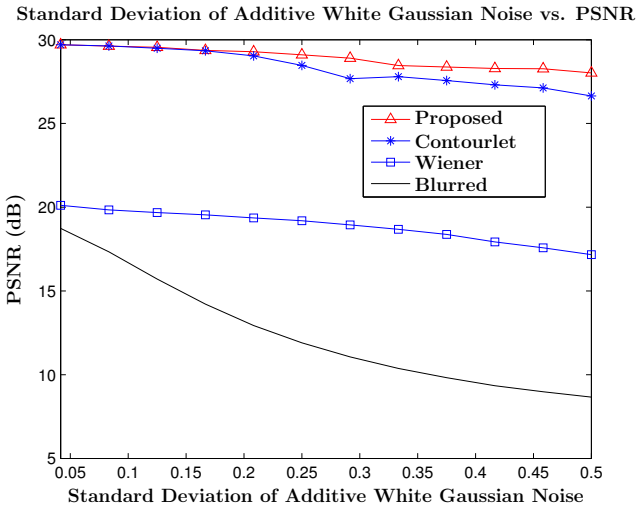

Figure 6.7: The proposed algorithm maintains a stable PSNR.

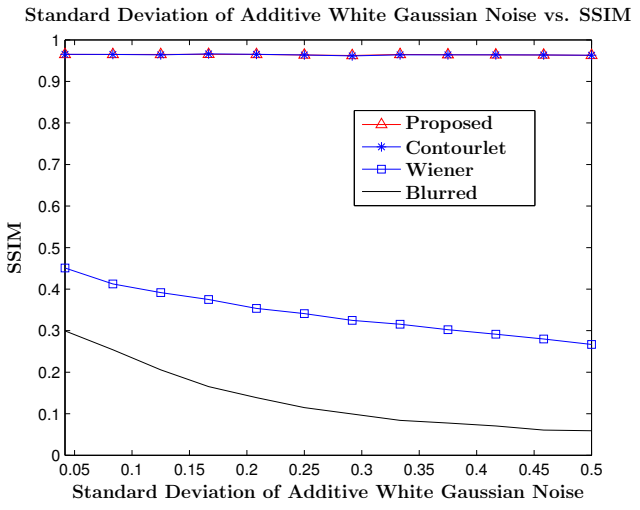

Figure 6.8: The proposed algorithm maintains a stable SSIM.

proposed algorithm is stable while the contourlet algorithm degrades. At these levels, the proposed algorithm achieves 0.5-1 dB gain over the contourlet method. In Fig. 6.8, the SSIM is the same between the two methods. Under large amounts of the noise, the shading of the two methods is different while the edge and structure information is similar.

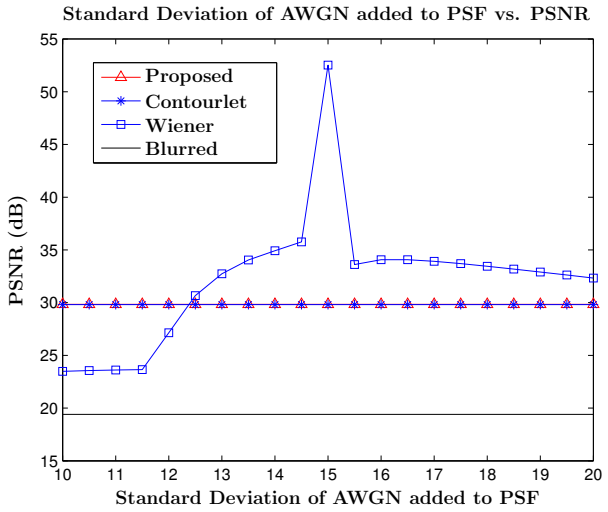

Figure 6.9: The noise affects the PSNR of Wiener deconvolution.

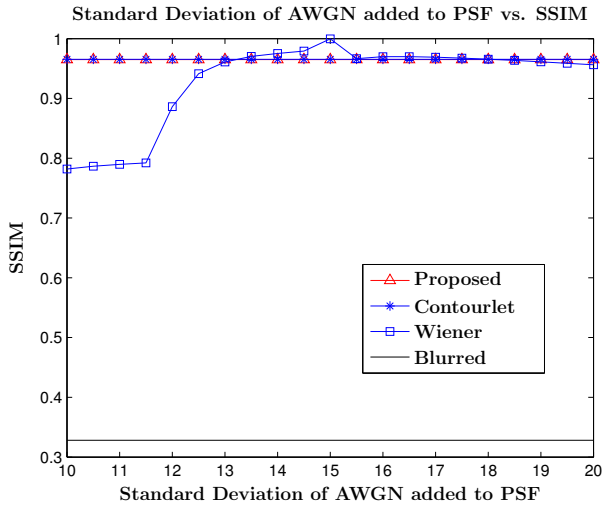

Figure 6.10: The noise affects the SSIM of Wiener deconvolution.

In Fig. 6.9 and Fig. 6.10, estimation error in the PSF is introduced to the system. For this test, an image is blurred with a Gaussian kernel of size 15x15 and

standard deviation 15. An alternate PSF is used during the deblurring phase. The alternate kernel is of size 15x15 and the standard deviation ranges from 10-20. To isolate the effects of noise in the PSF, no noise is added to the image.

When the standard deviation of the alternate kernel is at 10, the estimate of the PSF is poor and deblurring is not successful with Wiener deconvolution. In this region, the reconstruction error from the proposed method and the contourlet method is smaller than the Wiener method. When the standard deviation of the alternate kernel is 15, an exact match between the original and the alternate PSF is used. No noise is added to the system and no errors are produced by estimating the PSF. In this case, Wiener deconvolution is equivalent to inverse filtering and is the optimal solution. When the standard deviation is 20, Wiener deconvolution results are higher than the proposed method. The kernel size is 15x15, the kernel shape changes only slightly between kernel size 16 and kernel size 20. The alternate PSF in this case is a reasonable estimate of the original PSF.

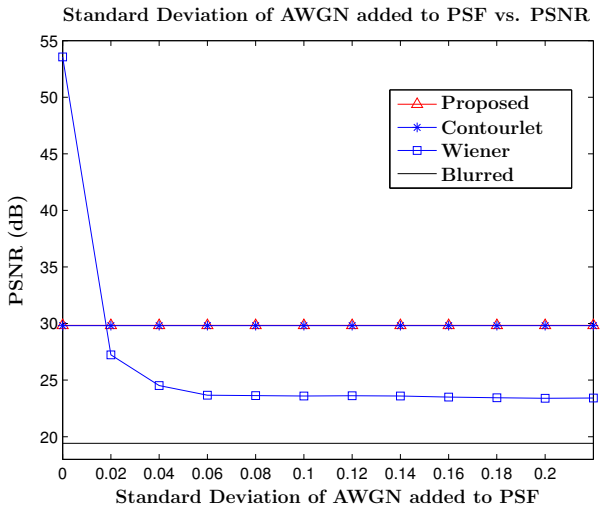

Figure 6.11: The noise affects the PSNR of Wiener deconvolution.

In Fig. 6.11 and Fig. 6.12, noise is added to the PSF and each algorithm is run. The goal of this test is to show which of the algorithms is robust to errors in estimating the PSF. In this test, the original image is blurred with a blur kernel of size 15x15 with standard deviation 15. An alternate PSF is used during the deblurring phase. The alternate PSF is created by adding noise to the original

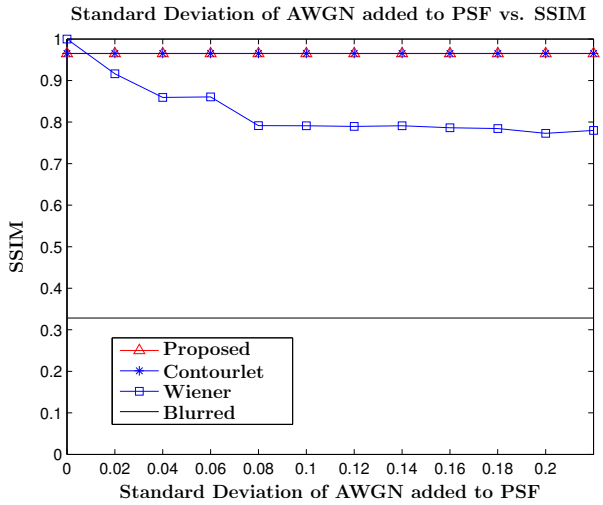

Figure 6.12: The noise affects the SSIM of Wiener deconvolution.

PSF. The noise is a 15x15 AWGN matrix with a standard deviation ranging from 0 to 0.2. A component-wise multiplication is performed between the original PSF and the AWGN matrix. After multiplication, the result is added to the original PSF to form a noisy estimate of the PSF. Wiener deconvolution is run with the noisy estimate of the PSF. Several regularization parameters were tested at each point and the highest PSNR and SSIM values are shown.

When the standard deviation of the AWGN added to the PSF is 0, no noise is contained in the estimate of the PSF. Wiener deconvolution is able to recover the original image and out performs all the other algorithms. Without any sources of noise, Wiener deconvolution is the optimal solution to the deblurring problem. The standard deviation of the AWGN added to the PSF is increased. Wiener deconvolution is dependent on an accurate PSF. The algorithm is affected dramatically by the increase in noise to the PSF. The proposed method and the contourlet method are robust to estimation errors in the PSF. A major advantage of these algorithms is that a PSF is not required. As the error increase, the PSNR and SSIM values of the Wiener method are worse than the values of the proposed and contourlet algorithms.

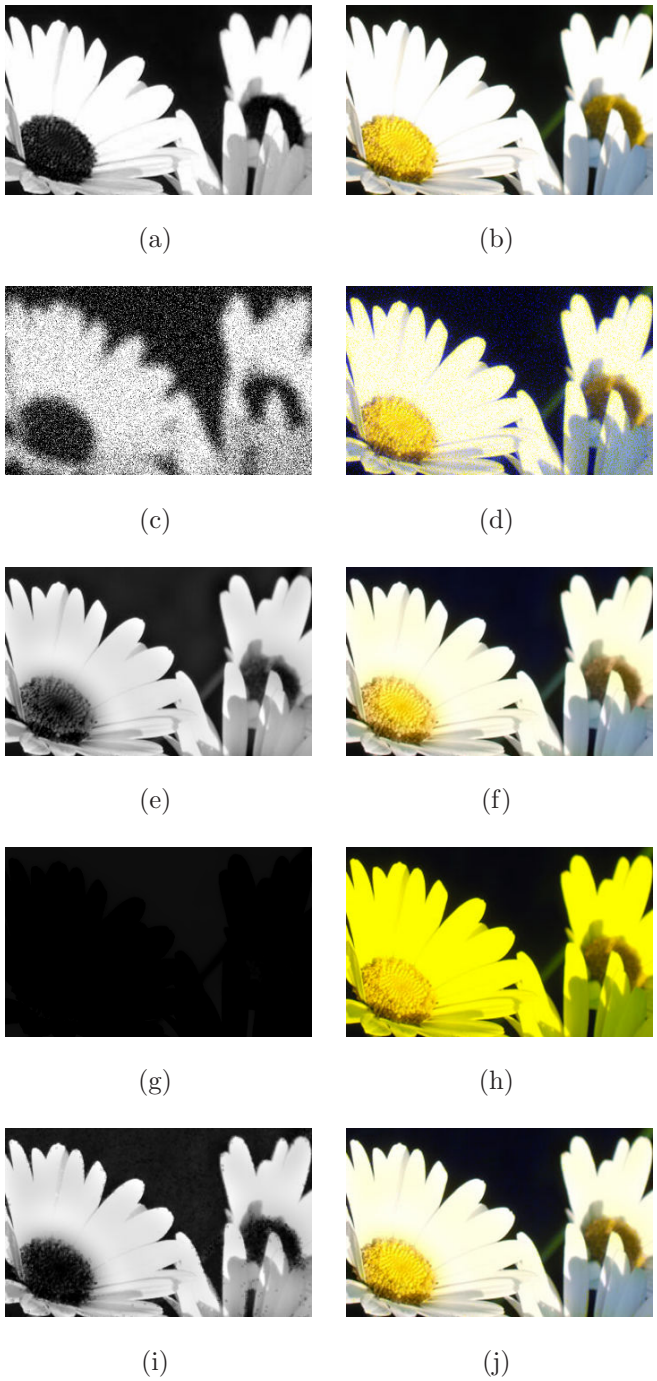

(a) (b) (c) (d) (e) (f) (g) (h) (i) (j)

Figure 6.13: Simulated blur and noise was added to these images. The color images must be viewed in color. (a) Original blue image; (b) original color image; (c) blurred and noisy blue image; (d) blurred and noisy color image; (e) Contourlet Sub-band Meshing blue image; (f) Contourlet Sub-band Meshing color image; (g) Color SVR blue image; (h) Color SVR color image; (i) proposed blue image; (j) proposed color image.

6.3.3 Natural Image Training Set

In Fig. 6.13, images are shown of a daisy flower. The goal of this simulation is to show that these ideas extend to other domains. For this set, the entire system was retrained using images of daisies. The Color SVR and Edge SVR were given new data points extracted from the daisy images. The Adaboost method was used to build a strong classifier on the daisy image data.

The domain of daisy images is different than the domain of the abdomen in a few key ways. In the abdomen domain, the edge correlation between green and blue pixels is high. The edges characteristics of the blue image are similar to the edge characteristics of the green image. In the daisy domain, green edge components are present that do not appear in the blue image. A poor match is produced between the edge components. Recovery of the correct blue image is not possible using the Contourlet Sub-band Meshing method.

The bud of the flower in Fig. 6.13(e) does not match the color of the original blue image. Using the Adaboost classification method, the problem of mismatched edges is reduced by the Color SVR. The classification is able to identify the regions where recovery of the green edges is possible using the Color SVR.

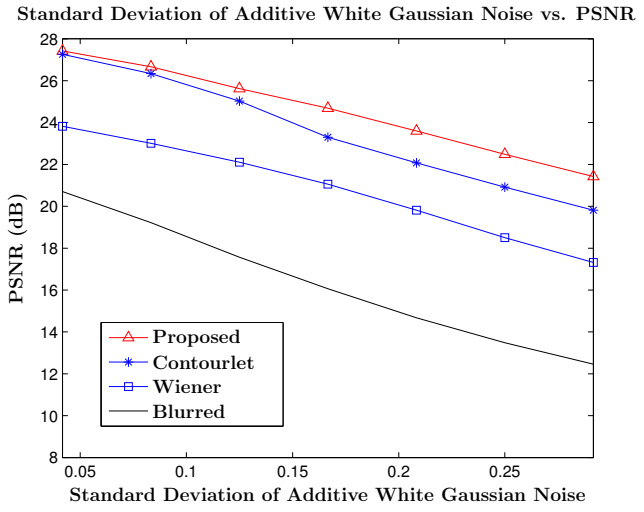

Figure 6.14: The proposed algorithm maintains a higher PSNR.

In Fig. 6.14 and Fig. 6.15, the results of adding AGWN to a daisy image are shown. In this test, a 15x15 Gaussian blur window with a standard deviation

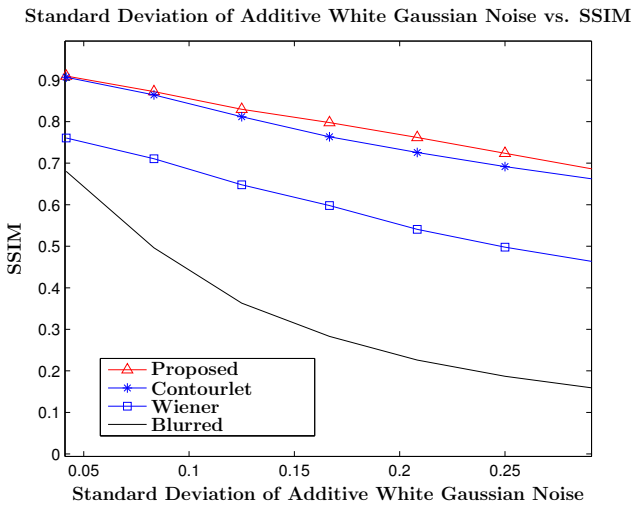

Figure 6.15: The proposed algorithm maintains a higher SSIM.

of 15 is used to blur the system. The standard deviation of the AWGN noise is increased. For this test, the models produced using the Daisy image set were applied. The contourlet algorithm begins to suffer because as more noise is added to the system, more of the green image edge coefficients are used. The green image edges are poorly correlated with the blue image edges. The shading values are altered significantly by the increase in green edge coefficients. The PSNR and SSIM values are lower as a result. The proposed algorithm is able to reduce this problem by using the Color SVR and Edge SVR models. The PSNR and SSIM are still affected by the increase is noise power.

6.3.4 Simulation Results from the Fluid Lens Camera

In Fig. 6.16, images taken from the device are presented. The FLCS was inserted into the abdomen of a pig. The abdomen was inflated and the FLCS was placed approximately 6 cm away from the object and was illuminated with a separate light source. The FLCS is a two lens system. The curvature of each lens is adjusted by filling and emptying the amount of liquid in the lens. By altering the curvature of the lens, the focus and magnification of the image is adjusted. More information about the testing set up can be found in [1].

In Fig. 6.16(c) and Fig. 6.16(e), the results of Lucy-Richardson and Wiener

deconvolution are shown. These images have fewer blurring artifacts than the original images from the device. However, the noise artifacts are still prominent in both results. The PSF for these two algorithms was estimated from the device. The effectiveness of these algorithms is limited by the estimation errors produced by this unique PSF. For the Lucy-Richardson algorithm, the damping parameter was set to 0.2 and 20 iterations were run. For the Wiener deconvolution, the noise to signal ratio was set to 0.06.

In Fig 6.16(g), the results of the Contourlet Sub-band Meshing algorithm are shown. By using the sharp green image, the edge information is extracted by the contourlet method. This information is applied to the blue sub-band. In Fig 6.16(i), the results of the proposed algorithm are shown. Compared to the contourlet algorithm, this image has the same level of sharpness. However, certain blurring and shading problems along the right side of the image are removed. The varying levels of blur and noise presented by the FLCS are dealt with effectively by the proposed algorithm.

In Fig. 6.17, a non-medical image from the device is examined. For this test, the camera was placed in a well lit room approximately 30 cm away from the object. The Lucy-Richardson and Wiener deconvolution methods were given the same parameters as in the example in Fig. 6.16.

Similar to the results of the butterfly simulation in Fig. 6.2, noise artifacts are shown in the proposed algorithm. An image is produced by the contourlet algorithm with sharp edges and a few color bleeding artifacts. However, the change in domain is not compensated for by the proposed method. The colors presented by this test are not seen in the human body, thus the poor predictions are produced by the Color SVR. Similarly, the strong classifier produced by Adaboost is tuned for abdominal image data. Different portions of the image are not correctly classified. Because of the change in domain, more accurate results are produced by the contourlet-based method.

The text of Chapter 6 is adapted from *Multiband Deblurring using Adaboost for Fluid Lens Cameras Based on Color Correlation*, Jack Tzeng, Yoav Freund, and Truong Nguyen, submitted April 2010, in preparation for *IEEE Transactions*

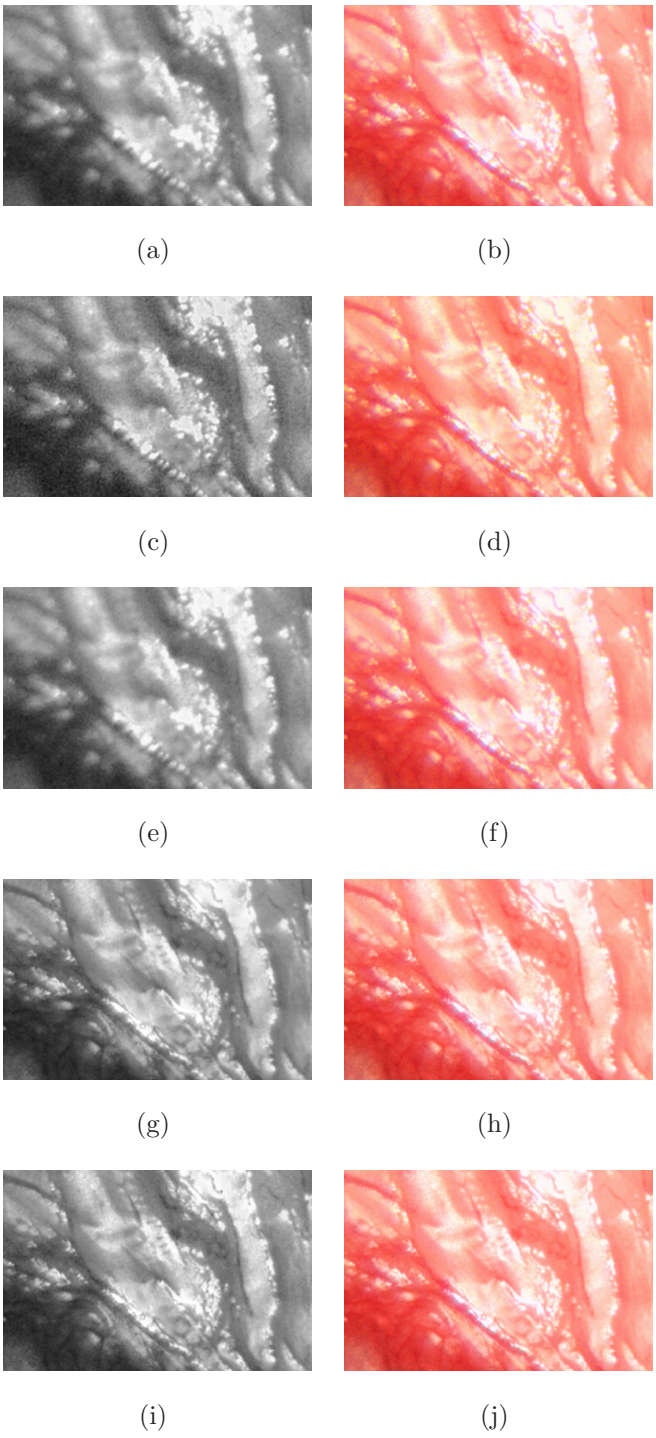

Figure 6.16: These image were taken using the FLCS. The color images must be viewed in color. (a) Original blue image; (b) original color image; (c) Wiener blue image; (d) Wiener color image; (e) Lucy-Richardson blue image; (f) Lucy-Richardson color image; (g) contourlet blue image; (h) contourlet color image; (i) proposed blue image; (j) proposed color image.

(a) (b)

(c) (d)

(e) (f)

(g) (h)

(i) (j)

Figure 6.17: These image were taken using the FLCS in a lab setting. The color images must be viewed in color. (a) Original blue image; (b) original color image; (c) Wiener blue image; (d) Wiener color image; (e) Lucy-Richardson blue image; (f) Lucy-Richardson color image; (g) contourlet blue image; (h) contourlet color image; (i) proposed blue image; (j) proposed color image.

on Image Processing. The dissertation author was the primary author of these publications, the first co-author listed supplied ideas, and the second co-author listed directed and supervised the research which forms the basis for this chapter.

Chapter 7

Conclusion

A viable and ground breaking technology is produced by the FLCS. The ability to miniaturize the lens and to achieve 5x zoom are presented by the system. A challenging area of research is the non-uniform color blurring caused by the lens.

The conventional Lucy-Richardson and Wiener deconvolution algorithms are outperformed by the proposed methods. Two more recent methods are also compared to the proposed methods: Dark Flash Photography and Total Variation. Information from infrared sensors is required for Dark Flash Photography. This additional requirement is not feasible for the FLCS because of the size restrictions of the lens body. Total Variation is also not feasible because an accurate estimate of the PSF is required.

In this work, four separate methods are explored:

Wavelet Sub-band Meshing

This algorithm is based on correlation of edges between color planes. The problem of a complicated PSF estimation is circumvented by this algorithm.

Contourlet Sub-band Meshing

In this method, directional filters are applied to adjust to the contours of the original image. Over the wavelet algorithm, color bleeding which occur when color edges exhibit weak correlation is reduced by this contourlet method.

SVR deblurring

In this method, different domains are utilized to extract the edge and shading

characteristics of a color image. After extraction, the edge and shading information are combined with a combination SVR. Medical image training data is used by this SVR in order to restrict the domain of possible outputs to only sharp medical images and colors found in the human body. Over previous methods, color bleeding is reduced in areas of weak edge correlation and performance is maintained in areas of strong edge correlation.

Adaboost classification

This method is a combination method. The results are combined from thee previous methods: the Contourlet Sub-band Meshing algorithm, the Color SVR, and the Edge SVR. Using Adaboost, a strong classifier is built to determine when each of the three algorithms will succeed. This classification is used to produce an image which has less error than the results from each of the three component methods.

The strengths of each algorithm are built upon while the challenges of the each algorithm are reduced. For a lens hardware solution to the color blurring problem, the intractable challenge of designing several surfaces in tandem is required. In order to improve the optical quality of the FLCS, viable solutions are proposed in the area of image processing. Overall, multiband solutions to the non-uniform blurring caused by the fluid lens are presented in this work.

7.1 Future Work

7.1.1 Improving proposed algorithms

As shown in Chapter 6, the Adaboost classification method has been shown to work on a set of daisy images and a set of abdominal images. One area of future research could be to develop training sets of other organs of the body such as the brain, heart, and lungs. Each domain may require unique image sets. A future area of work could be to explore the robustness of the algorithm to changes in lighting conditions, perspective, and location.

Another area of research is to expand the number of methods utilized by the Adaboost classification method. The current method compares three component algorithms to build one strong algorithm. Utilizing more than three algorithms may be able to improve results. One challenging issue is that Adaboost was originally developed as a two-class system. The current implementation accommodates three classes by using a cascade structure where two classes are initially compared and a third class is added. While the results appearing in this thesis are significant, generalizing this strategy to more than three classes may require exploration.

Features are a crucial component of the Adaboost method. The current implementation uses several surrounding derivatives in the color, spatial, and contourlet domain. This system could be improved by removing less important features and finding features which are more selective. In addition, reducing the total number features needed would dramatically improve the efficiency of the Adaboost algorithm.

7.1.2 Applying this work to other areas

The work discussed here may have broad applications in other fields of image processing. Satellite mapping, fluorescent medical imaging, and infrared imaging could all directly benefit from edge information sharing. Multi-resolution systems with several types of sensors could improve image fidelity by applying these techniques.

This work may also be applicable to compression. As shown in Chapter 6, the Adaboost algorithm and the Contourlet Sub-band Meshing algorithm are only slightly affected by significant amounts of noise and blur in the blue channel. Only a few number of low frequency components from the blue image are required. The edge components can be recovered by using the green image. A lossy encoding scheme may be able to utilize the redundancy in edge information to improve current compression techniques. These types of ideas are implicitly used in the YCrCb 4:2:2 standard which subsamples the chroma components by a factor of two. However, the proposed methods suggest that a much higher compression ratio can be achieved with only a slight degradation in image quality.

Bibliography

[1] Frank S. Tsai, Sung Hwan Cho, Yu-Hwa Lo, Bob Vasko, and Jeff Vasko, "Miniaturized universal imaging device using fluidic lens," *Optics Letters*, vol. 33, pp. 291–293, 2008.

[2] De-Ying Zhang, Nicole Justis, and Yu-Hwa Lo, "Integrated fluidic adaptive zoom lens," *Optical Letters*, vol. 29, no. 24, pp. 2855–2857, 2004.

[3] De-Ying Zhang, Nicole Justis, Victor Lien, Yevgeny Berdichevsky, and Yu-Hwa Lo, "High-performance fluidic adaptive lenses," *Applied Optics*, vol. 43, no. 4, pp. 783–787, 2004.

[4] Mario Bertero and Patrizia Boccacci, *Introduction to Inverse Problem in Imaging*, IOP Publishing Ltd., 1998.

[5] Augustus J. E. M. Janssen, "Extended nijboerzernike approach for the computation of optical point-spread functions," *Optical Society of America*, vol. Vol. 19, pp. 849–857, 2002.

[6] Alfred S. Carasso, "Linear and nonlinear image deblurring: A documented study," *SIAM Journal on Numerical Analysis*, vol. 36, pp. 1659–1689, 1999.

[7] William Hadley Richardson, "Bayesian-based iterative method of image restoration," *Journal of Optical Society of America*, vol. 62, no. 1, pp. 55–59, January 1972.

[8] L.B. Lucy, "An iterative technique for the rectification of observed distributions," *The Astronomical Journal*, vol. 79, no. 6, pp. 745–754, June 1974.

[9] Norbert Wiener, *Extrapolation,Interpolation,and Smoothing of Stationary Time Series*, The MIT Press, 1964.

[10] Jack Tzeng and Truong Nguyen, "Image enhancement for fluid lens camera based on color correlation," *IEEE Transactions on Image Processing*, vol. 18, no. 4, pp. 729–739, April 2009.

[11] Jack Tzeng and Truong Nguyen, "Using filter banks to enhance image for fluid lens cameras based on color correlation," in *IEEE International Conference on Acoustics,Speech,and Signal Processing*, April 2009.

[12] Bahadir K. Gunturk, Yucel Altunbasak, and Russell M. Mersereau, "Color plane interpolation using alternating projections," *IEEE Trans. on Image Processing*, vol. 11, pp. 997–1012, 2002.

[13] Bahadir K. Gunturk, John Glotzbach, Yucel Altunbasak, Ronald W. Schafer, and Russel M. Mersereau, "Demosaicking: Color filter array interpolation," in *IEEE Signal Processing Magazine*, 2005, vol. 44.

[14] James E. Adams Jr., "Interactions between color plane interpolation and other image processing functions in electronic photography," in *SPIE*, 1995, vol. 2416.

[15] Georges Henri Cottet and Mohamed El Ayyadi, "A volterra type model for image processing," *IEEE Transactions on Image Processing*, vol. 7, no. 3, pp. 292–303, March 1998.

[16] Jack Tzeng, Chun-Chen Liu, and Truong Nguyen, "Multi-band color image deblurring using contourlets for fluid lens camera systems," in *IEEE International Conference on Image Processing*, 2009.

[17] Minh N. Do and Martin Vetterli, *Beyond Wavelets*, chapter Contourlets, pp. 83–106, Academic Press, 2003.

[18] Minh N. Do and Martin Vetterli, "The contourlet transform: An efficient directional multiresolution image representation," *IEEE Trans. on Image Processing*, vol. 14, pp. 2091–2106, 2005.

[19] Ingrid Daubechies, *Ten Lectures on Wavelets*, Society for Industrial and Applied Mathematics (SIAM),Philadelphia,PA,1992 Capital City Press, 1992.

[20] Gilbert Strang and Truong Q. Nguyen, *Wavelets and Filter Banks*, Wellesley-Cambridge Press, 1997.

[21] Harris Drucker, Christopher J. C. Burges, Linda Kaufman, Alex J. Smola, and Vladimir Vapnik, "Support vector regression machines," in *NIPS*. 1996, pp. 155–161, MIT Press.

[22] Vladimir N. Vapnik, *The nature of statistical learning theory*, Springer-Verlag New York,Inc. New York,NY,USA, 1998.

[23] Leonid I. Rudin, Stanley Osher, and Emad Fatemi, "Nonlinear total variation based noise removal algorithms," *Phys. D*, vol. 60, pp. 259–268, 1992.

[24] Peter A. Jansson, Ed., *Deconvolution of Images and Spectra*, Academic Press, 2nd edition, 1997.

[25] James G. Nagy and Dianne P. O'Leary, "Restoring images degraded by spatially variant blur," *SIAM Journal on Scientific Computing*, vol. 19, pp. 1063–1082, 1998.

[26] Mark R. Banham and Aggelos K. Katsaggelos, "Digital image restoration," *IEEE Signal Processing Magazine*, vol. 14, no. 2, pp. 24–41, March 1997.

[27] Yilun Wang, Junfeng Yang, Wotao Yin, and Yin Zhang, "A new alternating minimization algorithm for total variation image reconstruction," *SIAM Journal on Imaging Sciences*, vol. 1, pp. 248272, 2008.

[28] Luciano Alparone, Lucien Wald, Jocelyn Chanussot, Claire Thomas, Paolo Gamba, and Lori Mann Bruce, "Comparison of pansharpening algorithms: Outcome of the 2006 grs-s data-fusion contest," *IEEE TRANSACTIONS ON GEOSCIENCE AND REMOTE SENSING*, vol. 45, pp. 3012–3021, 2007.

[29] Jorge Nunez, Xavier Otazu, Octavi Fors, Albert Prades, Vicenc Pala, and Roman Arbiol, "Multiresolution-based image fusion with additive wavelet decomposition," *IEEE TRANSACTIONS ON GEOSCIENCE AND REMOTE SENSING*, vol. 37, pp. 1204–1211, 1999.

[30] Javier Portilla, Vasily Strela, Martin J. Wainwright, and Eero P. Simoncelli, "Adaptive wiener denoising using a gaussian scale mixture model in the wavelet domain," in *International Conference on Imge Processing*, 2001.

[31] Javier Portilla, Vasily Strela, Martin J. Wainwright, and Eero P. Simoncelli, "Image denoising using scale mixtures of gaussians in the wavelet domain," *IEEE Transactions on Image Processing*, vol. 12, pp. 1338–1351, 2003.

[32] Javier Portilla, "Blind non-white noise removal in images using gaussian scale mixtures in the wavelet domain," in *IEEE Benelux Signal Processing Symposium*, 2004.

[33] Dilip Krishnan and Rob Fergus, "Dark flash photography," in *SIGGRAPH*, 2009.

[34] Michal Aharon, Michael Elad, and Alfred Bruckstein, "K-svd: An algorithm for designing of overcomplete dictionaries for sparse representation," *IEEE Transactions on Signal Processing*, vol. 54, pp. 4311–4322, 2006.

[35] Stefan Roth and Michael J. Black, "Fields of experts," *International Journal of Computer Vision*, vol. 82, pp. 205–229, 2005.

[36] Julian J. Mcauley, Tibrio S. Caetano, Alex J. Smola, and Matthias O. Franz, "Learning high-order mrf priors of color images," in *International Conference on Machine learning*, 2006.

[37] Barun Singh and William T. Freeman amd D. H. Brainard, "Exploiting spatial and spectral image regularities for color constancy," in *Workshop on Statistical and Computational Theories of Vision*, 2003, vol. 3.

[38] Ayan Chakrabarti, Keigo Hirakawa, and Todd Zickler, "Color constancy beyond bags of pixels," in *IEEE International Conference on Computer Vision and Pattern Recognition*, 2008.

[39] Xin Li, "Demosaicing by successive approximation," *IEEE Transactions on Image Processing*, vol. 14, no. 3, pp. 370–378, March 2005.

[40] A. Farras Abdelnour and Ivan W. Selesnick, "Nearly symmetric orthogonal wavelet bases," in *IEEE International Conference Acoustic,Speech,Signal Processing (ICASSP)*, May 2001, pp. 431–434.

[41] Duncan D.-Y. Po and Minh N. Do, "Directional multiscale modeling of images using the contourlet transform," *IEEE TRANSACTIONS ON IMAGE PROCESSING*, vol. 15, pp. 1610–1620, 2006.

[42] See-May Phoong, Chai W. Kim, P. P. Vaidyanathan, and Rashid Ansari, "A new class of two-channel biorthogonal filter banks and wavelet bases," *A New Class of Two-Channel Biorthogonal Filter Banks and Wavelet Bases*, vol. 43, pp. 649–665, 1995.

[43] Zhou Wang, Alan Conrad Bovik, Hamid Rahim Sheikh, and Eero P. Simoncelli, "Image quality assessment: From error visibility to structural similarity," *IEEE Transactions On Image Processing*, vol. 13, pp. 600–612, 2004.

[44] Pablo Arbelaez, Charless Fowlkes, and David Martin, *The Berkeley Segmentation Dataset and Benchmark*, U.C. Berkeley Computer Vision Group, June 2007, Images available at http://www.eecs.berkeley.edu/Research/Projects/CS/vision/bsds/.

[45] Allan Weber, *The USC-SIPI Image Database*, USC-SIPI, Images available at http://sipi.usc.edu/database/.

[46] Nello Cristianini and John Shawe-Taylor, *An introduction to support Vector Machines: and other kernel-based learning methods*, Cambridge University Press, New York,NY,USA, 2000.

[47] Bernhard Schölkopf, Alex J. Smola, Robert C. Williamson, and Peter L. Bartlett, "New support vector algorithms," *Neural Computation*, vol. 12, no. 5, pp. 1207–1245, 2000.

[48] Chih-Chung Chang and Chih-Jen Lin, *LIBSVM: a library for support vector machines*, 2001, Software available at www.csie.ntu.edu.tw/ cjlin/libsvm.

[49] Yoav Freund and Robert E. Schapire, "A short introduction to boosting," *Journal of Japanese Society for Artificial Intelligence*, vol. 14, pp. 771–780, 1999.

[50] D. D. Denison, M. H. Hansen, C. Holmes, B. Mallick, and B. Yu, Eds., *Nonlinear Estimation and Classification*, Springer, 2003.